Volume 21
Number 38
14 October 2025
Pages 7363–7574

Soft Matter

rsc.li/soft-matter-journal

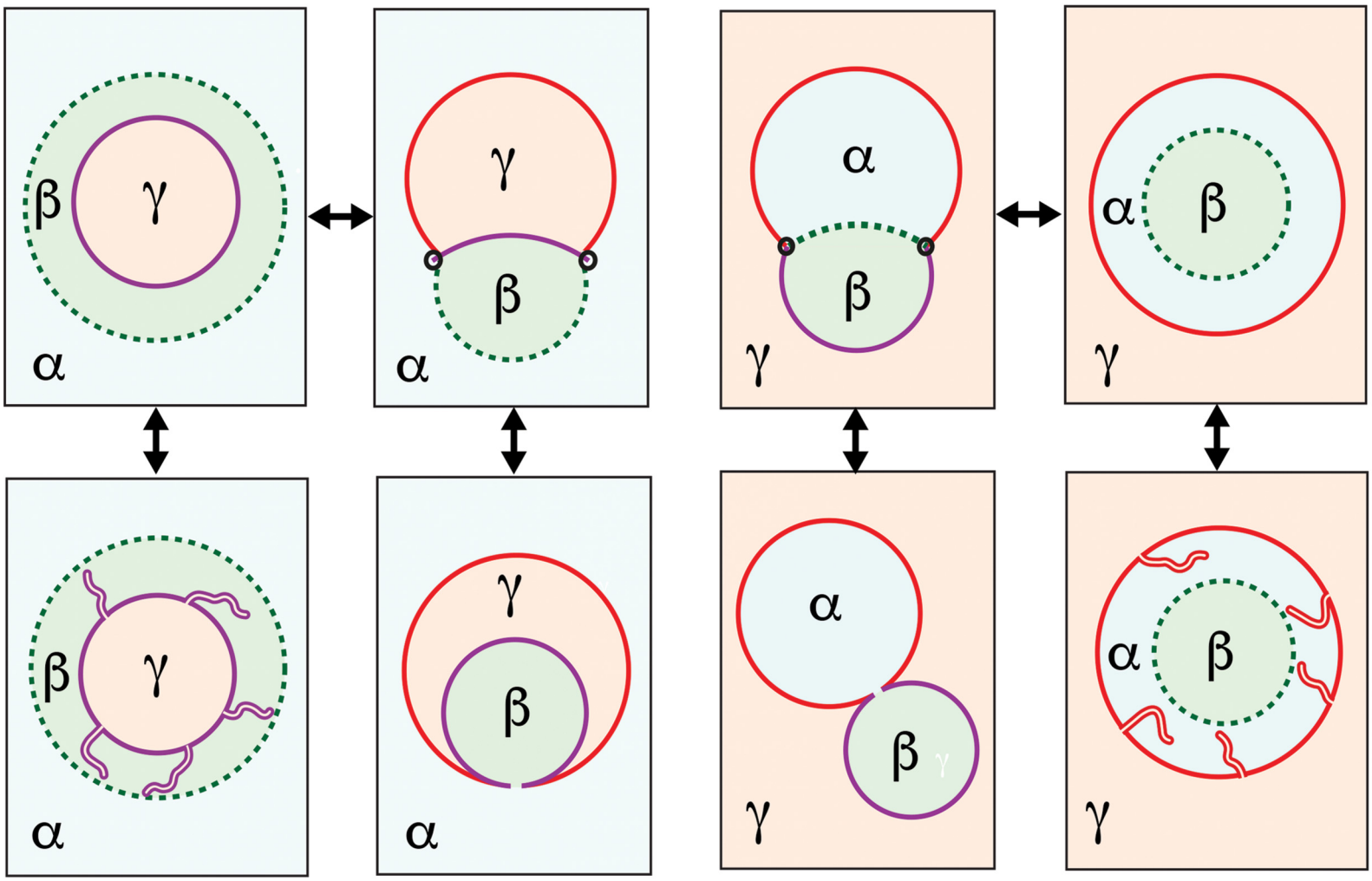

20 Years of Droplets and Vesicles

ISSN 1744-6848

ROYAL SOCIETY OF CHEMISTRY

PERSPECTIVE
Reinhard Lipowsky
Complex remodeling of biomembranes and vesicles by condensate droplets

20 YEARS ANNIVERSARY

Soft Matter

PERSPECTIVE

View Article Online
View Journal | View Issue

Cite this: *Soft Matter*, 2025, **21**, 7370

Complex remodeling of biomembranes and vesicles by condensate droplets†

Reinhard Lipowsky

Condensate droplets are formed by liquid–liquid phase separation in aqueous solutions of macromolecules such as polymers and proteins. Here, we look at the interactions of such droplets with biomembranes, integrating the results of recent experimental studies and computer simulations into the theoretical framework of fluid elasticity. The droplets can be formed *via* segregative or associative phase separation. It is argued that the corresponding phase diagrams exhibit one or two critical demixing points at constant temperature and that the vicinity of such a critical point leads to complete wetting of the membranes by the droplets. In general, both exterior and interior droplets can exhibit different wetting geometries, characterized by three apparent contact angles on the scale of a few hundred nanometers, as resolved by conventional light microscopy, and by two intrinsic contact angles on the scale of a few tens of nanometers. In response to a reduction of vesicle volume or to an increase of membrane area, the vesicle–droplet systems undergo a variety of remodeling processes, such as complete engulfment of the droplets or nanotubulation of the membranes. The closure of membrane necks adjacent to condensate droplets can proceed *via* several distinct morphological pathways. For partial wetting, the nanotubes adhere to the liquid–liquid interfaces and can then transform into double-membrane sheets.

Received 5th June 2025,
Accepted 16th July 2025

DOI: 10.1039/d5sm00585j

rsc.li/soft-matter-journal

1 Introduction

The term 'condensate droplet' as used here describes a droplet that is enclosed by a liquid–liquid rather than by a liquid–gas interface. Condensate droplets form in aqueous two-phase (or biphasic) systems, which have been applied in biochemical analysis and biotechnology[1] and are intimately related to water-in-water emulsions.[2,3] Here, we consider the interactions of such droplets with biomembranes and vesicles, which lead to complex membrane remodeling *via* capillary forces.[4–6] Experimentally, vesicle–droplet systems were first studied for aqueous PEG–dextran solutions interacting with giant vesicles.[7–9]

In this perspective, we will view membrane–droplet systems as biomimetic soft matter systems with unusual elastic and morphological properties as revealed by recent experimental studies[10–15] and molecular dynamics simulations.[16–18] To understand the behavior of these systems in a systematic and quantitative manner, we extend the theoretical framework of fluid elasticity, which involves two basic assumptions.[6] The first assumption is that the condensate droplets are enclosed by a liquid–liquid interface. The morphological behavior of such an interface is governed by its interfacial tension, which represents the main thermodynamic driving force of the membrane–droplet systems. The second assumption is that the biomembranes are in a fluid state which implies that their morphology is governed by a few curvature-elastic parameters such as bending rigidity and spontaneous (or preferred) curvature, in addition to the membrane tensions within the different membrane segments, which balance the interfacial tension.[4] Membrane tensions must be distinguished from interfacial tensions because they have fundamentally different properties. In particular, the thermodynamic route to membrane tensions is ill-defined in contrast to the thermodynamic definition of interfacial tensions.[19]

The framework of fluid elasticity also applies to the interactions of GUV membranes with coacervate droplets. Recent studies of these interactions include the formation of coacervate droplets within GUVs,[20,21] the exocytosis of such droplets from GUVs,[22,23] and the endocytosis and uptake of coacervate droplets by GUVs.[24] In addition, droplets of biomolecular condensates have also been observed in eukaryotic cells where they represent membraneless organelles, which are not enclosed by intracellular membranes. These condensate droplets form *via* liquid–liquid phase separation in the cytoplasm,[25,26] can be reconstituted *in vitro*,[12,27–29] and remodel cellular membranes *via* capillary forces.[30–34]

The paper is organized as follows. In Section 2, segregative and associative phase separation are distinguished in the

Max Planck Institute of Colloids and Interfaces, Science Park Golm, 14424 Potsdam, Germany. E-mail: lipowsky@mpikg.mpg.de

† Electronic supplementary information (ESI) available: Sections S1–S10; Fig. S1–S11; Table S1. See DOI: https://doi.org/10.1039/d5sm00585j

absence of membranes. Section 3 looks at complete and partial wetting of vesicle membranes by condensate droplets, arising from phase separation in the exterior and interior solutions. Changes in vesicle volume or membrane area (Section 4) lead to two alternative morphological pathways, complete engulfment of droplets and nanotubulation of membranes, as described in Sections 5 and 6, respectively. The fluid-elastic parameters, which control these pathways, are specified in Section 7 and then used in Section 8 to explain the competition between complete engulfment and nanotubulation.

Next, we discuss endocytosis of condensate droplets as observed in molecular dynamics simulations, thereby revealing the important role of the contact line tension, which can be positive or negative, see Section 9. The closure of membrane necks that are formed during the complete engulfment of droplets are examined in both Sections 9 and 10. Apparent contact angles are introduced in Section 11, where they are used to describe the force balance at the contact line. The corresponding force balance regime provides a two-dimensional parameter space for multiple transitions between distinct vesicle–droplet morphologies as explained in Section 12. Intrinsic contact angles are introduced in Section 11.3 and discussed in Section 12.6, reversible shape transformations between membrane nanotubes and nanosheets are examined in Section 13.

In the main text, most key points are explained by schematic drawings and by relatively short equations, focussing on simple relationships between the relevant fluid-elastic parameters. Some technical details can be found in the ESI.† The term ''giant vesicle'' always implies a ''giant unilamellar vesicle (GUV)''.

2 Segregative *versus* associative phase separation

Phase separation in aqueous solutions of polymers or proteins leads to the formation of two coexisting liquid phases. Depending on the underlying molecular interactions between the macromolecules, additional small solutes, and the water molecules, aqueous two-phase systems can be formed by segregative or associative phase separation.[2,3]

2.1 Two macromolecular species

When the aqueous solutions contain two different species of macromolecules, segregative phase separation leads to two aqueous phases, each of which is enriched in a different species. In contrast, associative phase separation leads to one phase enriched in both macromolecular species and another phase with a low concentration of the macromolecules. This different behavior implies effectively repulsive and attractive interactions between the different macromolecules for segregative and associative phase separation, respectively.[35]

2.2 One macromolecular species and salt

Aqueous phase separation is also observed for one macromolecular species and salt. To include this case, a different distinction between segregative and associative phase separation is introduced here, based on the number of critical demixing points within the phase diagram at constant temperature. The vicinity of a critical demixing point has a strong influence on the wetting behavior of condensate droplets at membranes and vesicles because it leads to complete wetting by one of the coexisting liquid phases, as described in Section 11.5 and depicted in Fig. 10a and 22 below.

2.3 One or two critical demixing points

For segregative phase separation, the phase diagram exhibits a single critical point at constant temperature. The classical example for this case is provided by aqueous solutions of PEG and dextran, see the segregative phase diagram[36] in Fig. S1 of Section S1 (ESI†). Similar phase diagrams are also obtained for a binary mixture of water and solute molecules[37] (Fig. S2, ESI†), for the PGL-1 protein *in vivo*[28] (Fig. S3, ESI†), and for aqueous solutions of PEG and potassium phosphate,[1,38] all of which exhibit a segregative phase diagram with a single critical demixing point at constant temperature. In contrast, associative phase separation leads to a constant-temperature phase diagram with two critical demixing points.

It seems that the distinction between segregative and associative phase separation has not been previously discussed in terms of the number of critical demixing points within the constant-temperature phase diagrams. However, this distinction is consistent with the phase diagrams of ternary liquid mixtures as displayed in ref. 2 and 3. Indeed, the tie lines shown in these phase diagrams imply one and two critical points for segregative and associative phase separation, respectively. Two examples for associative phase diagrams are provided by aqueous solutions of the soybean protein glycinin and sodium chloride[27] (Fig. 1) as well as of the FUS protein and potassium chloride[29] (Fig. 2).

2.4 Associative phase separation in aqueous solutions of the soybean protein glycinin and sodium chloride

Glycinin is one of the most abundant storage proteins of soybeans. Aqueous solutions of glycinin undergo liquid–liquid phase separation in the presence of sodium chloride.[27] The corresponding phase diagram is displayed in Fig. 1. This phase diagram exhibits a two-phase coexistence region (red) at intermediate salt concentrations. The two-phase region is bounded by two binodal lines. The shape of these binodals implies the presence of two critical points as indicated in Fig. 1. Close to these critical points, the tie lines across the two-phase region are nearly horizontal, corresponding to almost the same NaCl concentrations for the glycinin-poor and the glycinin-rich phase.

2.5 Associative phase separation in aqueous solutions of FUS protein and potassium chloride

A second example for associative phase separation is provided by aqueous solutions of the fused in sarcoma (FUS) protein and potassium chloride. The corresponding phase diagram is displayed in Fig. 2 as a function of molar protein concentration

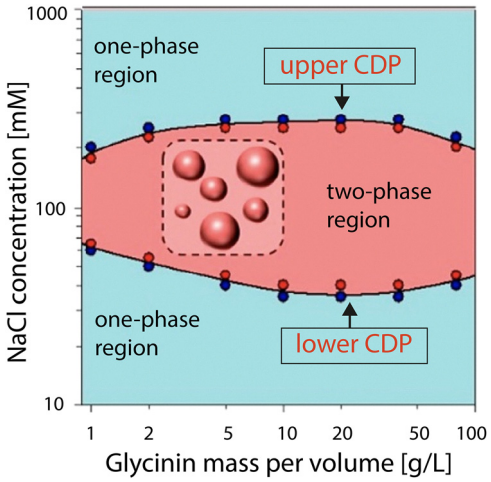

Fig. 1 Associative phase diagram for aqueous solutions of the soybean protein glycinin and sodium chloride at room temperature.[27] The coordinates of the two-dimensional phase diagram are given by the mass per volume concentration of glycinin and the molar concentration of NaCl. The solutions of glycinin and NaCl exhibit two one-phase regions (blue) separated by one two-phase region (red) at intermediate salt concentrations. The two-phase region is bounded by an upper and a lower binodal line, which exhibit an upper and a lower critical demixing point (CDP).

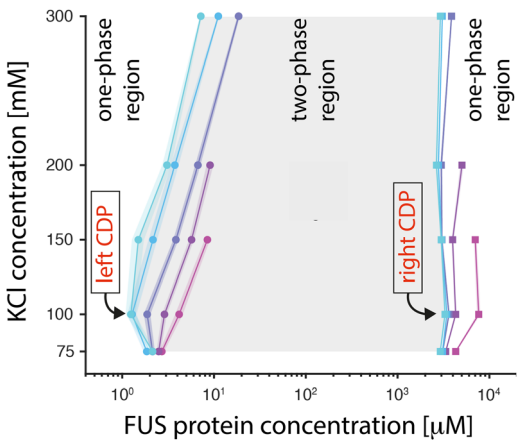

Fig. 2 Associative phase diagram for aqueous solutions of the FUS protein and potassium chloride at different temperatures.[29] The coordinates of the two-dimensional phase diagram are given by the molar concentration of fused in sarcoma (FUS) protein and the molar concentration of KCl. The different colors correspond to the binodals at different temperatures. At 15 °C, the two phase region is bounded by the darker blue binodals, which include a left and right critical demixing point (CDP).

and molar salt concentration.[29] The two critical demixing points are located at low salt concentrations.

3 Exterior and interior phase separation

Each vesicle membrane separates three-dimensional space into an interior and an exterior compartment. Both the exterior aqueous solution outside the vesicle and the interior aqueous solution inside the vesicle may undergo liquid–liquid phase separation. In both cases, the two coexisting liquid phases formed by the phase separation process will be denoted by α and β. These two phases are separated by an αβ liquid–liquid interface. In addition, the vesicle–droplet systems necessarily involve a third phase, denoted by γ, which does not participate in the aqueous phase separation and plays the role of an inert spectator phase.

3.1 Aqueous phase separation in the exterior solution

Aqueous phase separation in the exterior solution is illustrated in Fig. 3. In this example, the phase separation leads to the majority (or bulk) phase α and to the minority (or droplet) phase β. Depending on the molecular composition of the vesicle membrane and of the aqueous phases α, β, and γ, the membrane can be partially or completely wetted by the β phase as in Fig. 3. For complete wetting by a β droplet, the contact angle between the droplet's interface and the membrane vanishes whereas this angle has a finite value for partial wetting. This distinction applies to both the apparent contact angle as observed by conventional light microscopy and to the intrinsic contact angle on nanoscopic scales, see Section 11 below.

For partial wetting as shown in Fig. 3a, the membrane forms a contact line with the αβ interface, which pulls on the membrane *via* capillary forces and divides this membrane up into (i) an αγ segment (red) in contact with the α phase and (ii) a βγ segment (purple) exposed to the β droplet. The capillary forces exerted by the αβ interface lead to the apparent kink of the membrane shape along the contact line as depicted in Fig. 3a.[5]

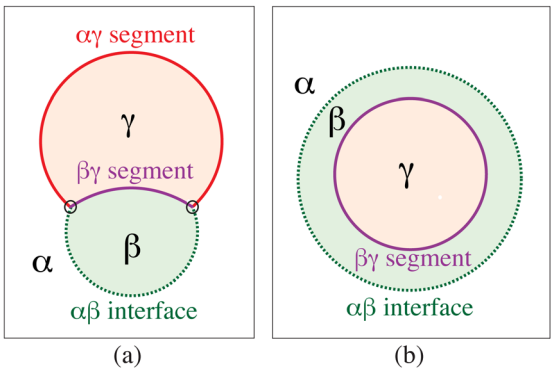

Fig. 3 Aqueous phase separation in the exterior solution with the majority phase α (white) and the minority phase β (green). The interior phase γ (pink) represents an inert spectator phase. The two coexisting phases α and β are separated by αβ interfaces (dotted green lines): (a) partial wetting of the vesicle membrane (red/purple) by an exterior β droplet. The αβ interface forms a contact line with the membrane and exerts capillary forces onto this membrane, which lead to apparent membrane kinks (small black circles). The contact line divides the membrane into two membrane segments, an αγ segment (red) exposed to the α phase and a βγ segment (purple) in contact with the β droplet; and (b) complete wetting of the vesicle membrane (purple) by an exterior β layer, which completely covers the membrane. As a consequence, the membrane is not exposed to the α phase and does not exhibit an αγ segment.

For complete (or perfect) wetting, on the other hand, the membrane is only in contact with one of the two coexisting phases α or β. In Fig. 3b, for instance, the membrane is only in contact with a wetting layer of β phase, which completely covers the membrane. In general, the vesicle–droplet system is predicted to exhibit complete wetting close to a critical demixing point, at which the interfacial tension $\Sigma_{\alpha\beta}$ of the αβ interface goes to zero, see Section S2 and Fig. S4 (ESI†). This prediction about complete wetting is explained in Section 11.5 below and has been experimentally confirmed both for segregative phase separation of PEG–dextran solutions (Fig. 10) and for associative phase separation of glycinin–NaCl (Fig. 22).

For a different composition of the exterior aqueous solution, the phase separation can also lead to a majority phase β and a minority phase α. The corresponding vesicle morphologies for partial wetting by an α droplet and for complete wetting by an α layer are obtained from Fig. 3a and b by swapping the α and β phases in both panels of this figure.

Complete wetting of the vesicle membrane by the β phase as in Fig. 3b is equivalent to complete dewetting of this membrane from the α phase. In other words, complete wetting by β implies an effectively attractive interaction of the membrane with the β droplet but an effectively repulsive interaction of the membrane with the α phase. Likewise, complete wetting by α and complete dewetting from β reveal effectively attractive and repulsive interactions of the membrane with α and β. Furthermore, attractive interactions of the membrane to the α phase can be transformed into attractive interactions to the β phase by changes in the salt concentration as observed for aqueous solutions of the soybean protein glycinin and sodium chloride, see Fig. 22 below.

3.2 Aqueous phase separation in the interior solution

Aqueous phase separation in the interior vesicle compartment is displayed in Fig. 4. In this case, the phase separation leads to two droplets, consisting of α and β phase, within the vesicle, which is surrounded by the exterior spectator phase γ. Depending on the molecular composition of the vesicle membrane, of the interior droplets α and β, and of the exterior spectator phase γ, the membrane can be partially wetted by both droplets or completely wetted by one of the two phases α and β as in Fig. 4a and b.

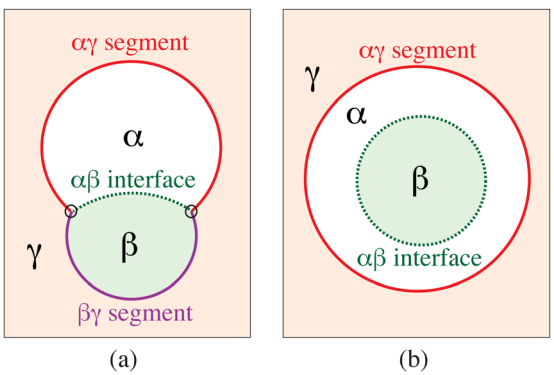

Fig. 4 Aqueous phase separation in the interior solution which leads to the coexisting phases α (white) and β (green), separated by αβ interfaces (dotted green lines). The exterior phase γ (pink) represents an inert spectator phase: (a) partial wetting of the vesicle membrane (red/purple) by the interior and β droplets. The αβ interface pulls on the membrane and divides this membrane into an αγ segment (red) and a βγ segment (purple); and (b) complete wetting of the vesicle membrane (red) by an interior α layer, which completely covers the membrane. As a consequence, the membrane is not in contact with the β droplet and does not exhibit a βγ membrane segment.

For partial wetting as shown in Fig. 4a, both interior droplets α and β are in contact with the vesicle membrane, forming a contact line with the αβ interface that exerts capillary forces onto the membrane and divides the membrane up into two segments, an αγ segment between the α and γ phase as well as a βγ segment between the β and γ phase. The capillary forces lead to the apparent membrane kink in Fig. 4a.

For complete wetting of the vesicle by the α phase as in Fig. 4b, the vesicle membrane is completely covered by a thin α layer, which is equivalent to complete dewetting of this membrane from the β phase. In other words, complete wetting by the α phase implies effectively attractive interactions of the membrane with the α droplet but effectively repulsive interactions of the membrane with the β droplet. Furthermore, vesicle–droplet morphologies with complete wetting by the β phase are also possible and can be obtained from Fig. 4b by swapping the α and β phases.

In aqueous PEG–dextran solutions, complete wetting of the vesicle membrane by the PEG-rich α phase as in Fig. 4b has been observed experimentally close to the critical demixing point, see Fig. 10a below.[10] Further away from this point, one observes partial wetting by both α and β as in Fig. 4b. The corresponding wetting regimes are displayed in Fig. S5 of Section S3 (ESI†).

4 Changes in vesicle volume or membrane area

The vesicle–droplet systems develop more complex morphologies *via* changes of the vesicle volume or the membrane area. A widely used method to change vesicle volume in a reversible manner is *via* the molar concentration of small solutes in the exterior solution. The vesicle volume is reduced by increasing this exterior solute concentration and increased by diluting this concentration. A simple but slow method to change the membrane area is *via* temperature changes. A fast and reversible method for area changes is provided by the addition of photo-responsive lipids that undergo conformational changes upon illumination with light of different wavelengths.[13,39,40]

Both processes change the geometry of the vesicle–droplet systems by reducing the dimensionless volume-to-area ratio $\bar{v}$, which is proportional to $V/A^{3/2}$ for a vesicle with volume V and membrane area A. Changes in the volume-to-area ratio lead to two alternative morphological transformations. First, the condensate droplet may be completely engulfed by the vesicle membrane, thereby eliminating the αβ interface from the vesicle–droplet system as in Fig. 5 and 6. Second, one of the

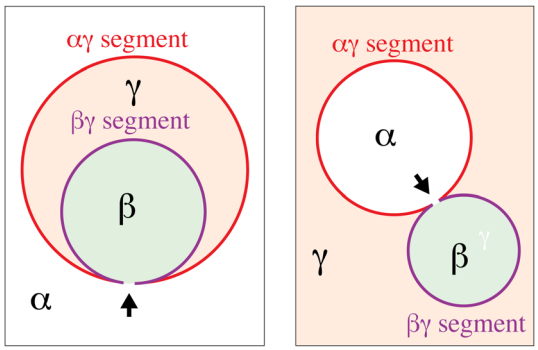

Fig. 5 Complete engulfment of condensate droplets by in- and out-buds of vesicle membranes: (a) endocytic engulfment of exterior β (green) droplet as obtained from Fig. 3a by reducing the vesicle volume; and (b) exocytic engulfment of interior droplets α (white) and β (green) as obtained from Fig. 4a. In both (a) and (b), complete engulfment leads to a narrow or closed membrane neck (black arrows), which eliminates the αβ interface from the vesicle–droplet system. Therefore, complete engulfment is facilitated by a large interfacial tension of the αβ interface.

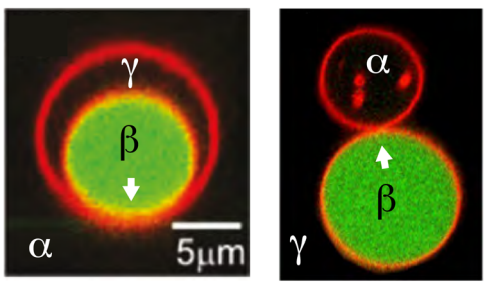

Fig. 6 Complete engulfment of condensate droplets by GUV membranes (red) as observed by confocal microscopy: (a) two-sphere shape of a GUV membrane, which completely engulfs the exterior dextran-rich β droplet (green) by an in-bud. The in-bud is connected to the outer membrane by a closed membrane neck (white arrow). Reused with permission of ref. 43, American Chemical Society, 2012. (b) Two-sphere shape of a GUV membrane, which forms two spherical segments around both the interior dextran-rich β (green) and the interior PEG-rich α (black) droplet, connected by a closed neck (white arrow). Reused with permission from ref. 44, John Wiley and Sons, 2017. These images correspond to the schematic drawings in Fig. 5.

membrane segments may form membrane nanotubes as in Fig. 7–10.

5 Complete engulfment of condensate droplets

For large interfacial tension $\Sigma_{\alpha\beta}$, the reduction of the volume-to-area ratio $\bar{v}$ of the vesicle leads to the complete engulfment of the condensate droplets by the vesicle membranes as depicted in Fig. 5, which illustrates the endocytic engulfment of an exterior droplet in panel (a) and the exocytic engulfment of the interior α and β droplets in panel (b).

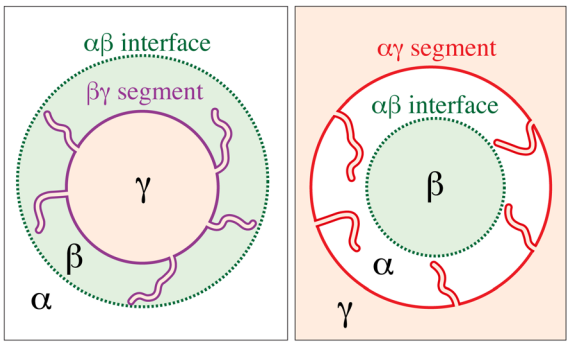

Fig. 7 Formation of membrane nanotubes for complete wetting: (a) exterior nanotubes (purple stubs) formed by the βγ membrane segment (purple) for complete wetting of the membrane by the β phase and large positive spontaneous curvature $m_{\beta\gamma}$ of the βγ segment; and (b) interior nanotubes (red stubs) formed by the αγ membrane segment (red) for complete wetting by the α phase and large negative spontaneous curvature $m_{\alpha\gamma}$ of the αγ segment. In both (a) and (b), the nanotubes are filled with γ phase and stay away from the αβ interface. For visual simplicity, all nanotubes are taken to be cylindrical even though they can also attain multispherical or unduloidal shapes.

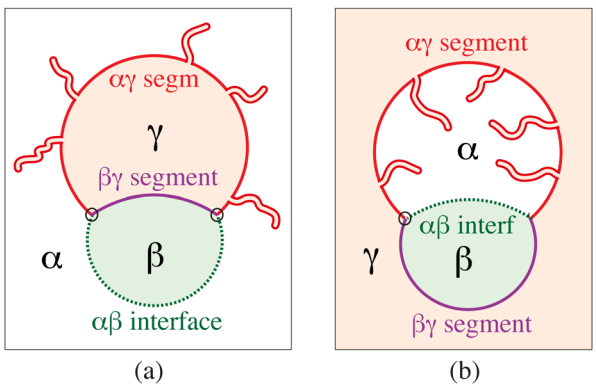

Fig. 8 Early stage of nanotube formation for partial wetting and a large spontaneous curvature $m_{\alpha\gamma}$ of the αγ segments: (a) outward-pointing nanotubes (red stubs) for large and positive spontaneous curvature $m_{\alpha\gamma} \gg A_{\alpha\gamma}{}^{-1/2}$, where $A_{\alpha\gamma}$ is the area of the αγ segment; and (b) inward-pointing nanotubes (red stubs) for large and negative spontaneous curvature $m_{\alpha\gamma} \ll -A_{\alpha\gamma}{}^{-1/2}$. As in Fig. 7, all tubes are filled with γ phase. At a later stage of the tubulation process, the nanotubes start to adhere to the αβ interface, see Fig. 9.

During complete engulfment, the open membrane necks in Fig. 3a and 4a become closed, which leads to a strong reduction of the interfacial area. On the nanoscale, one has to distinguish different pathways for the neck closure, see Sections 9 and 10. In the present section, we focus on the simplest case of contact line necks, for which the contact lines are located at the waistlines of the closing necks. This case is adequate for the order-of-magnitude estimates to be used in Section 8. For a contact line neck, complete engulfment reduces the free energy of the vesicle–droplet systems by the interfacial free energy $\Sigma_{\alpha\beta}A_{\alpha\beta}$, which depends on the interfacial tension $\Sigma_{\alpha\beta}$ and on the interfacial area $A_{\alpha\beta}$, both of which are positive.

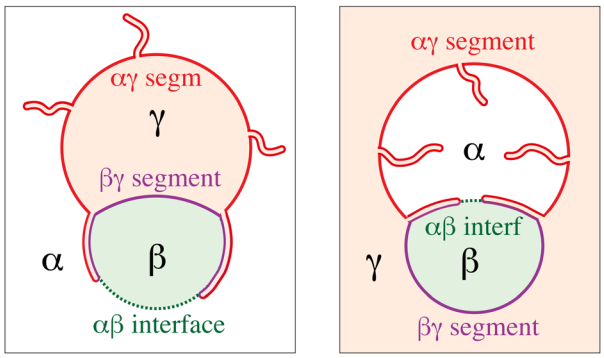

Fig. 9 When the membrane nanotubes come into contact with the αβ interfaces (dotted green lines), they adhere to these interfaces: (a) two outward-pointing nanotubes adhering to the αβ interface of the exterior β droplet; and (b) two inward-pointing nanotubes adhering to the αβ interface between the interior α and β droplets. As in Fig. 7 and 8, all tubes are filled with γ phase. As time goes one, more and more tubes adhere to the αβ interface. Each adhering nanotube consists of two membrane segments, one αγ (red) and one βγ (purple) segment.

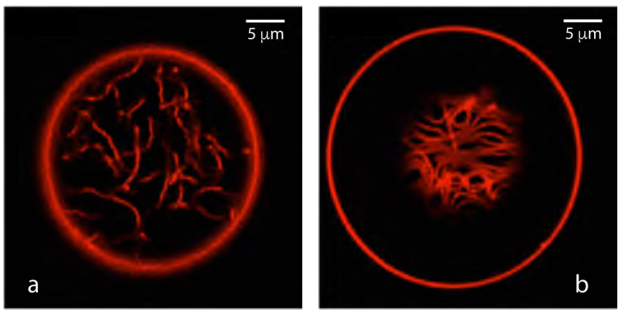

Fig. 10 Different patterns of membrane nanotubes formed by the αγ membrane segment (red) in contact with the PEG-rich phase α:[10] (a) disordered pattern corresponding to complete wetting of the vesicle membrane by the PEG-rich phase α as in Fig. 7b; and (b) nanotubes adhering to the underlying αβ interface for partial wetting of the membrane by both aqueous phases as in Fig. 9b. All tubes are connected to the outer vesicle membranes (big red circles). In both images, the diameter of the fluorescently labeled tubes (red line segments) is below the diffraction limit of the confocal microscope.

5.1 Geometric constraints for complete engulfment

The engulfment of condensate droplets by vesicle membranes involves three geometric parameters, which can be determined experimentally. For endocytic engulfment of an exterior droplet as in Fig. 5a, these geometric parameters are the volumes V_β and V_γ of the β and γ droplets enclosed by the vesicle as well as the total surface area $A = A_{\alpha\gamma} + A_{\beta\gamma}$ of the vesicle membrane. For exocytic engulfment as in Fig. 5b, these parameters are the volumes V_α and V_β of the α and β droplets inside the vesicle as well as the total membrane area A. Complete engulfment of the condensate droplet by the vesicle membrane is only possible for sufficiently large membrane areas or sufficiently small droplet volumes.

Complete engulfment of an exterior β droplet as shown in Fig. 5a is only possible if the droplet volume V_β and the total membrane area A fulfill the inequality[6,17]

$$A \geq 2(36\pi)^{1/3} {V_\beta}^{2/3} \quad \text{or} \quad V_\beta \leq \frac{A^{3/2}}{2^{3/2}(36\pi)^{1/2}}. \tag{1}$$

On the other hand, for complete engulfment of two interior α and β droplets as in Fig. 5b, it is necessary that the two droplet volumes V_α and V_β as well as the membrane areas $A_{\alpha\gamma}$ and $A_{\beta\gamma}$ with $A = A_{\alpha\gamma} + A_{\beta\gamma}$ satisfy

$$A \geq (36\pi)^{1/3}\left({V_\alpha}^{2/3} + {V_\beta}^{2/3}\right) \text{ and } V_\alpha + V_\beta \leq \frac{{A_{\alpha\gamma}}^{3/2} + {A_{\beta\gamma}}^{3/2}}{6\sqrt{\pi}}. \tag{2}$$

The two relationships in eqn (1) and (2) follow from the isoperimetric inequality ${A_o}^3 \geq 36\pi {V_o}^2$, which is valid for any closed surface in three dimensions[41,42] with surface area A_o and enclosed volume V_o. The limiting cases, in which these inequalities become equalities, correspond to the two-sphere shapes displayed in Fig. 5.

5.2 Complete engulfment by giant vesicle membranes

Complete engulfment of condensate droplets by giant vesicle membranes has been observed when these membranes were exposed to aqueous two-phase systems formed by PEG–dextran solutions. The resulting morphologies of the vesicle–droplet systems are displayed in Fig. 6, both for exterior and for interior phase separation.

6 Nanotubulation of vesicle membranes

For both exterior and interior phase separation, the two leaflets of the vesicle membranes are exposed to different aqueous solutions. This solution asymmetry contributes to the transbilayer asymmetry of the bilayer membranes and to their spontaneous curvature. A membrane segment with a sufficiently large spontaneous curvature can form nanotubes. For uniform membranes with a laterally uniform molecular composition, the mean curvature of these nanotubes is equal to the spontaneous curvature as follows from the theory of curvature elasticity[4,45,46] and has been scrutinized by several experimental studies.[9,10,47–49]

In addition, different molecular compositions of the α and β phases will generate different spontaneous curvatures, $m_{\alpha\gamma}$ and $m_{\beta\gamma}$, of the two membrane segments αγ and βγ. Each membrane segment can possess a positive or negative spontaneous curvature m.[4,10,45–48] A sufficiently large and positive spontaneous curvature $m_{\alpha\gamma}$ generates outward-pointing tubes of the αγ segment whereas a sufficiently large and negative spontaneous curvature $m_{\alpha\gamma}$ induces inward-pointing tubes of the αγ segment. The same distinction applies to the βγ segments, which form outward-pointing tubes for large and positive $m_{\beta\gamma}$ and inward-pointing tubes for large and negative $m_{\beta\gamma}$.

After their formation, the nanotubes exhibit spatial patterns that are different for complete and partial wetting of the vesicle membranes. The tubular patterns are relatively simple for

complete wetting but undergo a complex time evolution for partial wetting.

6.1 Nanotubulation for complete wetting

The nanotube patterns for complete wetting are shown in Fig. 7a and b for aqueous phase separation in the exterior and interior solution, respectively. In both cases, the nanotubes are filled with the spectator phase γ.

All membrane segments in Fig. 7a represent βγ segments, with their outer and inner leaflets in contact with the β and γ phase, respectively. These βγ segments form nanotubes for sufficiently large and positive spontaneous curvatures $m_{\beta\gamma}$. On the other hand, all membrane segments in Fig. 7b correspond to αγ segments, with their inner and outer leaflets exposed to the α and γ phase, respectively. These αγ segments form nanotubes for sufficiently large and negative spontaneous curvatures $m_{\alpha\gamma}$.

6.2 Nanotubulation for partial wetting

For partial wetting, the vesicle membrane is exposed to both phases α and β as in Fig. 3a and 4a. In addition, the two leaflets of the αγ and of the βγ membrane segments are exposed to distinct aqueous solutions and, thus, will exhibit different spontaneous curvatures $m_{\alpha\gamma}$ and $m_{\beta\gamma}$. In general, both spontaneous curvatures can be positive or negative, depending on the molecular composition of the adjacent aqueous phases. If one of these spontaneous curvatures has a sufficiently large absolute value, the corresponding membrane segment forms nanotubes.

6.2.1 Early stages of nanotubulation for partial wetting. When the spontaneous curvature $m_{\alpha\gamma}$ of the membrane segment αγ is sufficiently large and exceeds the spontaneous curvature $m_{\beta\gamma}$ of the βγ segment, the reduction of vesicle volume leads to nanotubes formed by the αγ segment. The width of these tubes is set by the inverse spontaneous curvature $1/|m_{\alpha\gamma}|$. Initially, several tubes are formed by different subsegments of the αγ membrane segment as shown in Fig. 8.

In both panels of Fig. 8, the tubes protrude towards the α phase which implies a positive spontaneous curvature, $m_{\alpha\gamma} > 0$, for the exterior α phase in Fig. 8a and a negative spontaneous curvature, $m_{\alpha\gamma} < 0$, for the interior α droplet in Fig. 8b.

6.2.2 Adhesion of nanotubes to αβ interface. The nanotubes are quite flexible and undergo thermally excited shape fluctuations, by which they eventually come into contact with the αβ interface. For partial wetting as in Fig. 8, each nanotube can lower its free energy by adhering to the αβ interface as depicted in Fig. 9 for some of these tubes.[10] Therefore, as time goes on, the nanotubes in Fig. 8 and 9 move towards the αβ interface until all nanotubes are eventually located at this interface.

6.2.3 Different shapes of nanotubes. For visual simplicity, the nanotubes in Fig. 7–9 are taken to have a cylindrical shape but can, in general, also attain unduloidal and multispherical shapes, as described in Section S4 and depicted in Fig. S6 (ESI†) for freely suspended nanotubes. Likewise, nanotubes adhering to the αβ interface can also have different shapes as schematically shown in Fig. 26 below.

6.3 Nanotubulation of giant vesicle membranes

Nanotubulation of giant vesicle membranes has been observed experimentally when the vesicles were exposed to aqueous PEG–dextran solutions. For interior phase separation, osmotic deflation of the giant vesicles generated two different patterns of nanotubes, corresponding to complete and partial wetting of the vesicle membrane as in Fig. 10. These different patterns of nanotubes are quite useful from an experimental point of view because they directly distinguish complete from partial wetting and also reveal the position of the αβ interface for partial wetting.

To understand why the osmotic deflation of giant vesicles, which are exposed to aqueous PEG–dextran solutions, develop two very different morphologies, complete engulfment and nanotubularion, as displayed in Fig. 6 and 10, we need to consider the different fluid-elastic parameters that govern the vesicle–droplet systems in more detail.

7 Fluid-elastic parameters of droplets and vesicles

7.1 Interfacial tension of condensate droplets

The main fluid-elastic parameter of a condensate droplet is provided by the interfacial tension $\Sigma_{\alpha\beta}$ of the αβ interface enclosing the droplet. This tension has been measured for aqueous solutions of PEG and dextran over a wide range of polymer concentrations.[36] These solutions undergo segregative phase separation into a PEG-rich phase α and a dextran-rich phase β for relatively low polymer concentrations. The corresponding phase diagram is displayed in Fig. S1 (ESI†) as a function of the two weight fractions w_d and w_p for dextran and PEG. When we move across this phase diagram of PEG–dextran two-phase systems, the interfacial tension $\Sigma_{\alpha\beta}$ varies over four orders of magnitude, from 10^{-4} mN m^{-1} to 1 mN m^{-1} as shown in Fig. S4 (ESI†). The data in this figure also imply that the interfacial tension vanishes in a continuous manner according to the power law $\Sigma_{\alpha\beta} \sim \Delta c^{\mu}$ as one approaches the critical demixing point at $\Delta c = 0$, with the critical exponent μ being close to its mean-field value[50] $\mu = 3/2$.

7.2 Curvature-elastic parameters of vesicle membranes

The elastic properties of uniform vesicle membranes are determined by two curvature-elastic parameters, the bending rigidity κ and the spontaneous curvature m. The bending rigidity κ describes the resistance of the membrane against bending. For phospholipid bilayers, a typical value for the bending energy, which has the physical dimension of energy, is $\kappa \simeq 10^{-19}$ J or $\kappa \simeq 20 k_B T$ at room temperature. The spontaneous curvature m describes the preferred membrane curvature arising from the underlying transbilayer asymmetry of the bilayer membranes. Depending on the molecular mechanism for this asymmetry,

the spontaneous curvature can vary over a wide range, see Section S5 and Table S1 (ESI†).

The bending rigidity κ and the spontaneous curvature m define the curvature-elastic (or spontaneous) tension[4,46]

$$\sigma \equiv 2\kappa m^2 \tag{3}$$

which represents the intrinsic tension scale of curvature elasticity. Inspection of Table S1 (ESI†) reveals that the curvature-elastic tension σ varies over seven orders of magnitude, depending on the lipid composition of the vesicle membranes and the solutes in the adjacent aqueous solutions.

7.3 Curvature-elastic parameters of membrane segments

For partial wetting of the vesicle membrane, the contact line with the αβ interface divides this membrane up into two segments, the αγ and the βγ segments as in Fig. 3a and 4a. The αγ membrane segment has bending rigidity $\kappa_{\alpha\gamma}$ and spontaneous curvature $m_{\alpha\gamma}$ whereas the βγ membrane segment has bending rigidity $\kappa_{\beta\gamma}$ and spontaneous curvature $m_{\beta\gamma}$. Furthermore, both membrane segment can be characterized by their curvature-elastic tensions as given by

$$\sigma_{\alpha\gamma} \equiv 2\kappa_{\alpha\gamma} {m_{\alpha\gamma}}^2 \quad \text{and} \quad \sigma_{\beta\gamma} \equiv 2\kappa_{\beta\gamma} {m_{\beta\gamma}}^2. \tag{4}$$

These two curvature-elastic tensions will, in general, attain different values within the range provided by the third row of Table S1 (ESI†).

Furthermore, the two membrane segments αγ and βγ will, in general, have different Gaussian curvature moduli $\kappa_{G,\alpha\gamma}$ and $\kappa_{G,\beta\gamma}$. For uniform membranes, both experimental studies[48,51,52] and computer simulations[53] have shown that the Gaussian curvature modulus is negative with an absolute value that is comparable to the bending rigidity. Therefore, for the two membrane segments αγ and βγ, we will use the estimates $\kappa_{G,\alpha\gamma} \simeq -\kappa_{\alpha\gamma}$ and $\kappa_{G,\beta\gamma} \simeq -\kappa_{\beta\gamma}$. The Gaussian curvature moduli affect the position of the contact line during the formation of a closed membrane neck as discussed in Section 10 and Fig. 14 below.

7.4 Line tension of contact line

At the nanoscale, the vesicle–droplet morphology also depends on the line tension λ_{cl} of the contact line. More precisely, the contact line tension becomes significant for sufficiently short contact lines, when their length L_{cl} fulfills the inequality

$$L_{cl} \lesssim L_{cl}^* \equiv \frac{|\lambda_{cl}|}{\Sigma_{\alpha\beta}} \tag{5}$$

with the threshold value L_{cl}^* depending on the absolute value of the contact line tension, $|\lambda_{cl}|$, and on the interfacial tension $\Sigma_{\alpha\beta}$. It is important to note that the interfacial tension $\Sigma_{\alpha\beta}$ is always positive whereas the contact line tension λ_{cl} can be positive or negative, see Section S6, Fig. S8 (ESI†), and Section 9 below.

7.5 Fluid elasticity and molecular length scales

The theory of fluid elasticity is based on a coarse-grained description, in which both the lipid bilayers and the liquid–liquid interfaces are regarded as fluid surfaces, largely ignoring the details of their molecular structure. The bilayers have a thickness of about 4 nm, corresponding to twice the length of the lipid molecules. The thickness of the αβ interface is usually set by the size of the largest macromolecules present in the liquid mixture but becomes much larger close to a critical demixing point, where the interface thickness is set by the diverging bulk correlation length. Furthermore, the width of the contact line is expected to be comparable to the thickness of the αβ interface.

8 Complete engulfment *versus* nanotubulation

As previously described in Sections 5 and 6, the reduction of the volume-to-area ratio $\bar{v}$ can lead to complete engulfment of the droplet by the vesicle membrane as in Fig. 5 and 6 or, alternatively, to nanotubulation of this membrane as in Fig. 7–10. Which morphological pathway is taken by the vesicle–droplet system depends primarily on the relative magnitude of the interfacial tension $\Sigma_{\alpha\beta}$ and the curvature-elastic tensions $\sigma_{\alpha\gamma}$ and $\sigma_{\beta\gamma}$ as explained in the following paragraphs.

8.1 Reduction of interfacial free energy by engulfment

When the area $A_{\alpha\beta}$ of the αβ interface with interfacial tension $\Sigma_{\alpha\beta}$ is reduced by $\Delta A_{\alpha\beta}$, the interfacial free energy of the vesicle–droplet system decreases by

$$\Delta E_{int} = -\Sigma_{\alpha\beta}\Delta A_{\alpha\beta}. \tag{6}$$

The interfacial tension is a material parameter, which depends on temperature and on the molecular composition of the α and β phases but is independent of the size and shape of the interface. For complete engulfment of the β droplet by the vesicle membrane as in Fig. 5 and 6, the αβ interface can be completely eliminated from the vesicle-droplet system, thereby reducing its free energy by $\Sigma_{\alpha\beta}A_{\alpha\beta}$ with the total interfacial area $A_{\alpha\beta}$.

8.2 Reduction of bending energy by tubulation

For a large spontaneous curvature $m_{\alpha\gamma}$ and a small mean curvature of the αγ membrane segment, this segment has a large bending energy of the order of $\sigma_{\alpha\gamma}A_{\alpha\gamma}$ which is proportional to the curvature-elastic tension $\sigma_{\alpha\gamma}$ of the αγ segment and to the surface area $A_{\alpha\gamma}$ of this segment. Now, when the membrane area $\Delta A_{\alpha\gamma}$ of the weakly curved mother vesicle is transferred into a nanotube of mean curvature $M \simeq m_{\alpha\gamma}$, we gain the bending energy

$$\Delta E_{be} = -\sigma_{\alpha\gamma}\Delta A_{\alpha\gamma} = -2\kappa_{\alpha\gamma}{m_{\alpha\gamma}}^2\Delta A_{\alpha\gamma}. \tag{7}$$

We now repeat this argument for the membrane segment βγ in contact with the aqueous phase β, which generates the spontaneous curvature $m_{\beta\gamma}$ of the βγ segment. When the membrane area $\Delta A_{\beta\gamma}$ of this segment forms a nanotube with mean curvature $M \simeq m_{\beta\gamma}$, we gain the bending energy

$$\Delta E_{be} = -\sigma_{\beta\gamma}\Delta A_{\beta\gamma} = -2\kappa_{\beta\gamma}{m_{\beta\gamma}}^2\Delta A_{\beta\gamma}. \tag{8}$$

8.3 Competition between interfacial and curvature-elastic tensions

The reduction of the membrane's bending energy by nanotube formation as given by eqn (7) and (8) remains to be compared with the reduction of the interfacial free energy by the engulfment of the droplet as described by eqn (6). We then conclude that complete droplet engulfment will be observed for[5]

$$\Sigma_{\alpha\beta} \gg \max[\sigma_{\alpha\gamma},\sigma_{\beta\gamma}] \quad \text{(complete engulfment)}. \qquad (9)$$

that is, when the interfacial tension $\Sigma_{\alpha\beta}$ is large compared to the curvature-elastic tensions $\sigma_{\alpha\gamma}$ and $\sigma_{\beta\gamma}$ of the membrane segments $\alpha\gamma$ and $\beta\gamma$, provided the geometric constraints for complete engulfment as given by eqn (1) and (2) can be fulfilled.

On the other hand, the membrane segment with the larger curvature-elastic tension can form nanotubes if

$$\max[\sigma_{\alpha\gamma},\sigma_{\beta\gamma}] \gg \Sigma_{\alpha\beta} \quad \text{(nanotube formation)}, \qquad (10)$$

that is, if the curvature-elastic tension of one of the membrane segments is large compared to the interfacial tension $\Sigma_{\alpha\beta}$, again provided the vesicle geometry allows the formation of nanotubes with a mean curvature that is equal to the spontaneous curvature of the respective membrane segment.

8.4 Nanotubulation close to critical demixing points

At a critical demixing point of the aqueous two-phase system, the interfacial tension $\Sigma_{\alpha\beta}$ goes to zero whereas the curvature-elastic tensions $\sigma_{\alpha\gamma}$ and $\sigma_{\beta\gamma}$ will attain finite values. Therefore, as we approach such a critical point, the vesicle–droplet system will eventually satisfy eqn (10) and sufficiently large vesicle membranes can then form membrane nanotubes as observed for the segregative phase separation of PEG–dextran solutions, see Fig. 10a and Fig. S5 (ESI†).

8.5 Nanotubulation after complete engulfment

For glycinin-rich β droplets in aqueous two-phase systems of glycinin and NaCl, nanotubulation of the $\alpha\gamma$ membrane segment has been observed after the complete engulfment of the β droplets (Section S7 and Fig. S9, ESI†).[13] The engulfment process was induced by a sufficiently large interfacial tension $\Sigma_{\alpha\beta}$, which satisfies eqn (9), and the subsequent nanotubulation of the $\alpha\gamma$ segment by a sufficiently large curvature-elastic tension $\sigma_{\alpha\gamma}$. This two-step process was driven by the alternating illumination of the vesicle with UV and blue light, which induces conformational transitions of azo-PC lipids within the vesicle membranes as shown in Fig. 24 below.

9 Endocytosis of condensate droplets

Complete engulfment of condensate droplets by vesicle membranes leads to a closed membrane neck as depicted by the black and white arrows in Fig. 5 and 6. The formation of a closed membrane neck adjacent to an exterior droplet represents the first step for the endocytic uptake of these droplets into the vesicles. The second step of endocytosis is the fission of this neck.

As shown in Fig. 6, complete engulfment by giant vesicle membranes has been observed for phase-separated PEG–dextran solutions within giant vesicles. The engulfment process led to two spherical subcompartments, with one subcompartment enclosing the PEG-rich α droplet whereas the other subcompartment was filled with the dextran-rich β droplet. However, these two subcompartments remained connected by a membrane nanotube (or "tether"), which implies that the membrane neck did not undergo fission.[44,54]

In contrast, complete engulfment followed by neck fission has been observed in molecular dynamics simulations as described in the following. In addition, these simulations also revealed that the closed membrane neck can attain an unusual tight-lipped shape that prevents the fission of this neck.[16,17]

9.1 Adhesion of condensate droplets to nanovesicles

The adhesion of an exterior condensate droplet to a nanovesicle as observed in molecular dynamics simulations is shown in Fig. 11. The adhesion geometry involves again three liquid phases as in Fig. 3a: the two coexisting phases α and β in the exterior solution as well as the inert spectator phase γ within the vesicle. After the onset of adhesion, the exterior droplet starts to spread over the membrane as in Fig. 11b, which leads to partial engulfment of the droplet by the membrane as in Fig. 11c. As before, the contact area of droplet and membrane defines the $\beta\gamma$ segment of the membrane while the membrane segment exposed to the α phase represents the $\alpha\gamma$ segment. The size of the $\beta\gamma$ segment depends on the relative size of droplet and vesicle.

9.2 Axisymmetric engulfment followed by vesicle division

During the partial engulfment process displayed in Fig. 11, the vesicle volume is kept constant and the $\beta\gamma$ segment in contact with the β droplet grows by pulling out excess membrane area that is stored in the thermally-excited shape fluctuations of the

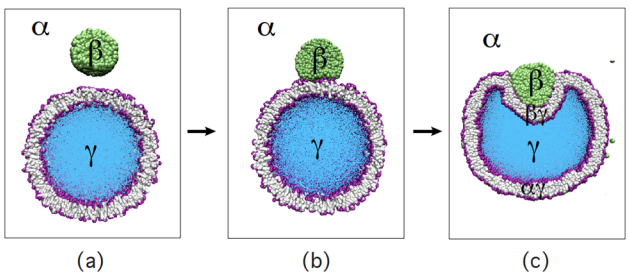

Fig. 11 Partial engulfment of an exterior condensate droplet (green) by the lipid bilayer (purple-grey) of a nanovesicle.[17] The vesicle encloses the aqueous spectator phase γ (blue). Both the nanodroplet and the nanovesicle are immersed in the aqueous bulk phase α (white): (a) initially, the droplet is well separated from the vesicle which implies that the outer leaflet of the bilayer is only in contact with the α phase; (b) when the droplet is attracted towards the vesicle, it spreads onto the lipid bilayer, thereby increasing its contact area with the vesicle; and (c) partial engulfment of the droplet by the membrane after the vesicle–droplet system has relaxed to a new stable state.

vesicle membrane. To further increase the contact area, one has to reduce the vesicle volume, which is filled with the blue spectator phase γ. Such a volume reduction leads to complete engulfment of the droplet by the vesicle membrane, provided the droplet volume is sufficiently small compared to the vesicle volume, see eqn (1), which applies to Fig. 11c. For a completely engulfed droplet, the area of the membrane segment βγ in contact with the droplet is equal to the surface area of the droplet and the αβ interface is replaced by a closed membrane neck, see the snapshot at time t = 4 μs in Fig. 12.

9.3 Tight-lipped shape of membrane neck

The complete engulfment of the droplet can also proceed in a non-axisymmetric manner and then leads to a strongly non-circular contact line and to a tight-lipped shape of the closed membrane neck as shown in Fig. 13.[17] The tight-lipped shape of the closed neck prevents the fission of this neck. Such an unusual neck shape was first observed for the complete engulfment of condensate droplets by planar bilayers.[16] Tight-lipped membrane necks are also formed during the endocytosis of rigid nanoparticles.[18]

9.4 Positive and negative contact line tensions

The two morphological pathways in Fig. 12 and 13 are controlled by the sign of the contact line tension, which can be positive or negative, as discussed in Section S6 and displayed in Fig. S8a (ESI†). For positive values of the line tension λ_{cl}, the engulfment of the condensate droplet proceeds in an axisymmetric manner and leads to the fission of the membrane neck as in Fig. 12. In contrast, for negative values of the line tension λ_{cl}, the condensate droplet is engulfed in a non-axisymmetric manner, which leads to a tight-lipped shape of the closed membrane neck[16,17] as in Fig. 13.

In addition, the simulations also show that the positive or negative sign of the contact line tension is primarily determined by the transbilayer stress asymmetry between the two leaflets of the bilayer membrane. Indeed, inspection of Fig. S8b (ESI†) reveals that the line tension is positive and negative for sufficiently large and small values of the transbilayer stress asymmetry, respectively.[17]

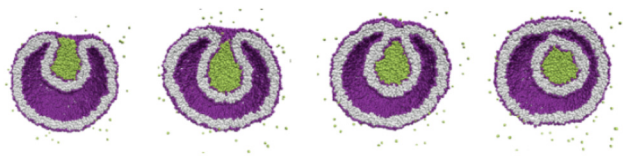

Fig. 12 Endocytosis of an exterior condensate droplet (green) *via* axisymmetric engulfment, followed by the division of the nanovesicle (purple-grey) into two nested daughter vesicles. At time t = 0, the droplet is partially engulfed by the vesicle membrane, which forms an open membrane neck. At t = 4 μs, the neck closes and the droplet becomes completely engulfed. The neck undergoes fission at t = 9 μs, generating a small intraluminal vesicle enclosing the droplet. The vesicle membrane contains N_{ol} = 5500 lipids in its outer and N_{il} = 4600 lipids in its inner leaflet. Such an axisymmetric process is observed for a positive line tension, $\lambda_{cl} > 0$, of the contact line.[17]

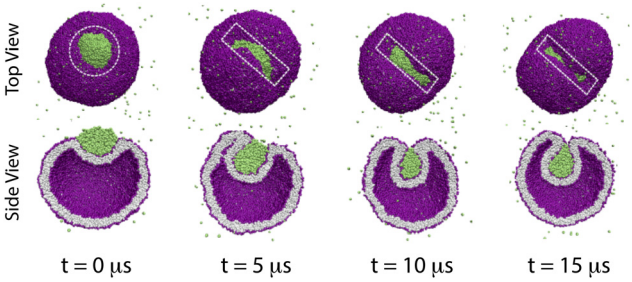

Fig. 13 Non-axisymmetric engulfment of an exterior condensate droplet (green), leading to a tight-lipped shape of the membrane neck that prevents neck fission: vesicle bilayer (purple-grey) with N_{ol} = 5963 lipids in its outer and N_{il} = 4137 lipids in its inner leaflet. At t = 0, the droplet is partially engulfed by the vesicle membrane with an axisymmetric contact line, as indicated by the white dashed circle. The axial symmetry is broken at t = 5 μs, as follows from the strongly non-circular and highly elongated contact lines for $t \geq 5$ μs, as indicated by the white dashed rectangles. Such a non-axisymmetric process is created by a negative line tension, $\lambda_{cl} < 0$, of the contact line.[17]

10 Distinct morphological pathways for the axisymmetric closure of membrane necks

As shown in Fig. 5 and 6, the complete engulfment of condensate droplets involves the formation of a closed membrane neck adjacent to such a droplet. Furthermore, for positive and negative contact line tension λ_{cl}, the formation of a closed neck can proceed in an axisymmetric and non-axisymmetric manner as described in the previous section, see Fig. 12 and 13. We will now further elucidate the closure of membrane necks adjacent to condensate droplets and show that such a neck closure process can proceed *via* several distinct axisymmetric pathways. For all pathways to be discussed in the following, the vesicle volume and the membrane area are taken to fulfill the geometric requirements for complete engulfment as described by eqn (1) and (2), thereby avoiding the stalling of the neck closure process by droplets that are too large to be enclosed by the vesicle membranes.

10.1 Axisymmetric closure of membrane neck

Let us first assume that the neck closes in an axisymmetric manner as expected for a positive contact line tension $\lambda_{cl} > 0$. This assumption implies that both the waistline of the membrane neck and the contact line have a circular shape. The corresponding radii are denoted by R_{ne} and R_{cl}. Furthermore, any axisymmetric vesicle shape can be parametrized by the arc length s of its shape contour, see Section S8 and Fig. S10 (ESI†). The contact line and the neck's waistline are then located at $s = s_{cl}$ and $s = s_{ne}$, respectively.

10.1.1 Discontinuity of mean curvature at contact line. For an axisymmetric vesicle consisting of two membrane segments, the theory of curvature elasticity predicts that the membrane's

mean curvature exhibits a discontinuity along the contact line if the αγ and βγ membrane segments differ in their curvature-elastic properties.[5] This discontinuity can be expressed in terms of the mean curvatures $M_{\alpha\gamma}(s_{cl})$ and $M_{\beta\gamma}(s_{cl})$ of the αγ and βγ segments at the two sides of the contact line and then has the form

$$\kappa_{\beta\gamma}\left[M_{\beta\gamma}(s_{cl}) - m_{\beta\gamma}\right] - \kappa_{\alpha\gamma}\left[M_{\alpha\gamma}(s_{cl}) - m_{\alpha\gamma}\right] = \frac{1}{2}\left[\kappa_{G,\alpha\gamma} - \kappa_{G,\beta\gamma}\right] C_{\parallel}(s_{cl}) \quad (11)$$

where $C_{\parallel}(s_{cl})$ is the principal curvature parallel to the contact line, which varies continuously across this line, and $\kappa_{G,\alpha\gamma}$ and $\kappa_{G,\beta\gamma}$ are the Gaussian curvature moduli of the two membrane segments as introduced before.

During the closure of the axisymmetric membrane neck, the neck radius R_{ne} goes to zero and the principal curvature $C_{\parallel}(s_{ne}) = 1/R_{ne}$ parallel to the neck's waistline diverges in the limit of small R_{ne}. We will first consider a "contact line neck", for which the contact line is located at the neck's waistline, which implies that the radius R_{cl} of the contact line is equal to the neck radius R_{ne}. As a consequence, the parallel principal curvature $C_{\parallel}(s_{cl}) = 1/R_{cl}$ of the contact line becomes equal to $1/R_{ne}$ and diverges as well when the neck closes. In order to elucidate the closure of such a contact line neck, we need to consider the energy of the corresponding two-droplet vesicle.

10.1.2 Energy of two-droplet vesicle with a closing neck. For a closed contact line neck with $R_{ne} = R_{cl} = 0$, the two-droplet vesicle becomes a two-sphere vesicle, as displayed in Fig. 5. The energy E_{2Sph} of this two-sphere vesicle is given by eqn (S17) in Section S8 (ESI†). When the contact line neck with $R_{cl} = R_{ne}$ has a small but finite radius, the energy of the two-droplet vesicle has the form

$$E_{2Dr}(R_{ne}) \approx E_{2Sph} + \zeta_{be}R_{ne} + 2\pi\lambda_{cl}R_{ne} + E_{\alpha\beta}(R_{ne}) \quad (12)$$

with the bending energy term $\zeta_{be}R_{ne}$, a term proportional to the contact line tension λ_{cl}, and the interfacial free energy[5]

$$E_{\alpha\beta}(R_{ne}) \equiv \Sigma_{\alpha\beta}A_{\alpha\beta} = \frac{2\pi}{1+\sin\theta_{\alpha}^{*}}\Sigma_{\alpha\beta}{R_{ne}}^{2} \quad (13)$$

The first-order term $\zeta_{be}R_{ne}$ in eqn (12) arises from the bending energy of the closing neck and defines the force ζ_{be} that contributes to the constriction force f at the closed neck as given by

$$f \equiv \left.\frac{\partial E_{2Dr}}{\partial R_{ne}}\right|_{R_{ne}=0} = \zeta_{be} + 2\pi\lambda_{cl}. \quad (14)$$

The force term ζ_{be} depends on the curvature-elastic parameters of the two membrane segments αγ and βγ and has a somewhat different parameter dependence for endocytic and exocytic necks in Fig. 5a and b, as given by eqn (S19) and (S20) in Section S8 (ESI†). The third term on the right-hand side of eqn (12) is also of first order in R_{ne} and represents the line free energy of the contact line, which is proportional to the contact line tension λ_{cl} (Section 9 and Section S6, ESI†). For a closed contact line neck with $R_{ne} = R_{cl} = 0$, both first-order terms contribute to the constriction force.

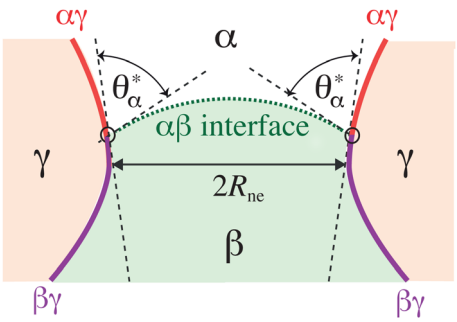

Fig. 14 Axisymmetric membrane neck (purple/red) spanned by a small segment of the αβ interface (dotted green), which has the shape of a spherical cap and forms the intrinsic contact angle θ_α^* with the αγ membrane segment (red). The radius R_{cl} of the circular contact line exceeds the radius R_{ne} of the circular waistline of the neck. Such a displacement of the contact line away from the neck's waistline, which is formed by the βγ segment (purple), represents one possible pathway for the axisymmetric neck closure when the two membrane segments have different Gaussian curvature moduli $\kappa_{G,\alpha\gamma}$ and $\kappa_{G,\beta\gamma}$ with $\kappa_{G,\alpha\gamma} < \kappa_{G,\beta\gamma}$.

The interfacial free energy $E_{\alpha\beta}$ in eqn (13) arises from the αβ interface, which forms a spherical cap across the closing neck and meets the membrane along the circular contact line with radius $R_{cl} = R_{ne}$ for a contact line neck. The energy $E_{\alpha\beta}$ is of second-order in the neck radius R_{ne} and proportional to the interfacial tension $\Sigma_{\alpha\beta}$. This energy also depends on the intrinsic contact angle θ_α^* between the αβ interface and the membrane segment αγ, see Fig. 14 and Section 11.3 below.

A careful analysis of the energy E_{2Dr} of the two-droplet vesicle as given by eqn (12) and the curvature discontinuity in eqn (11) then leads to several distinct morphological pathways for the axisymmetric closure of a contact line neck.

10.2 Neck closure for identical Gaussian curvature moduli

For identical Gaussian curvature moduli $\kappa_{G,\alpha\gamma}$ and $\kappa_{G,\beta\gamma} = \kappa_{G,\alpha\gamma}$, the right-hand side of eqn (11) vanishes, which leads to the simplified relation

$$\kappa_{\beta\gamma}[M_{\beta\gamma}(s_{cl}) - m_{\beta\gamma}] = \kappa_{\alpha\gamma}[M_{\alpha\gamma}(s_{cl}) - m_{\alpha\gamma}] \quad (15)$$

for the curvature discontinuity. The relation in eqn (15) no longer involves any term that diverges in the limit of small neck radius R_{ne}. Furthermore, if the membrane segments αγ and βγ have identical bending rigidities and spontaneous curvatures, eqn (15) further simplifies and reduces to $M_{\beta\gamma}(s_{cl}) = M_{\alpha\gamma}(s_{cl})$, corresponding to a continuous variation of the mean curvature across the contact line as studied in ref. 55.

For vesicles with two intramembrane domains, numerical solutions of the shape equations have shown that identical Gaussian curvature moduli of the two domains lead to an axisymmetric domain boundary with radius R_{db} that remains located at the membrane neck until $R_{ne} = R_{db} = 0$.[56] For two-domain vesicles, the closure of the domain-boundary neck is governed by two equations that are completely analogous to eqn (11) and (12), if one takes into account that the two-domain

vesicles do not involve an αβ interface, which implies $E_{\alpha\beta} = 0$.[57] Therefore, the contact line of an axisymmetric two-droplet vesicle with identical Gaussian curvature moduli $\kappa_{G,\alpha\gamma}$ and $\kappa_{G,\beta\gamma}$ of the two membrane segments will remain located at the membrane neck until the neck has been closed with $R_{ne} = R_{cl} = 0$.

For different Gaussian curvature moduli, we will now describe two additional pathways for which the neck closes in an axisymmetric manner but avoids the divergence of the parallel principal curvature $C_{\parallel}(s_{cl}) \sim 1/R_{cl} = 1/R_{ne}$ as follows from eqn (11) for a contact line neck.

10.3 Neck closure for positive constriction force

The first additional pathway is obtained by displacing the contact line away from the closing membrane neck, which implies that the membrane neck is no longer a contact line neck. The contact line then attains a finite radius R_{cl} in the limit of zero neck radius $R_{ne} = 0$. The interfacial free energy is still given by eqn (13) provided we replace the neck radius R_{ne} by the contact line radius R_{cl}. Likewise, the line free energy of the contact line is now equal to $2\pi\lambda_{cl}R_{cl}$. As a consequence, both the interfacial free energy and the line free energy in eqn (16) become independent of the neck radius R_{ne} and the closed neck with $R_{ne} = 0$ is primarily stabilized by the energy term $\zeta_{be}R_{ne}$ with a positive constriction force $f = \zeta_{be} > 0$.

The displacement of the contact line away from the closing neck is illustrated in Fig. 14 for $\kappa_{G,\alpha\gamma} < \kappa_{G,\beta\gamma}$. Because these moduli are related to the bending rigidities *via* $\kappa_{G,\alpha\gamma} \simeq -\kappa_{\alpha\gamma}$ and $\kappa_{G,bg} \simeq -\kappa_{\beta\gamma}$, the inequality $\kappa_{G,\alpha\gamma} < \kappa_{G,\beta\gamma}$ implies the inequality $\kappa_{\beta\gamma} < \kappa_{\alpha\gamma}$. The closing neck is then formed by the βγ membrane segment with the less negative Gaussian curvature modulus and the smaller bending rigidity, as follows from the analogous behavior of domain boundary necks in ref. 56.

10.4 Neck closure for negative constriction force

The second additional pathway is obtained for a negative constriction force, $f = \zeta_{be} + 2\pi\lambda_{cl} < 0$. The energy $E_{2Dr}(R_{ne})$ of the two-droplet vesicle as given by eqn (12) then becomes

$$E_{2Dr}(R_{ne}) = E_{2Sph} - |f|R_{ne} + c_{\alpha\beta}\Sigma_{\alpha\beta}R_{ne}^{2} \qquad (16)$$

with $c_{\alpha\beta} \equiv 2\pi/(1+\sin\theta_{\alpha}^{*}) > 0$. The energy in eqn (16) exhibits a local minimum at

$$R_{ne} = \frac{|f|}{2c_{\alpha\beta}\Sigma_{\alpha\beta}} = \frac{|\zeta_{be} + 2\pi\lambda_{cl}|}{2c_{\alpha\beta}\Sigma_{\alpha\beta}}. \qquad (17)$$

corresponding to a narrow neck with finite radius $R_{ne} > 0$.

Such a morphological pathway for neck closure has been observed for giant vesicles enclosing one PEG-rich and one dextran-rich droplet as displayed in Fig. 15.[44] The elongation of the membrane neck into a long membrane nanotube has also been observed in ref. 54 where the nanotubes were denoted as "tethers". This morphological pathway is unique to contact line necks of two-droplet vesicles and is not possible for domain boundary necks of two-domain vesicles.[56,57] Indeed, the latter vesicles do not involve an αβ interface and their energy does not include the interfacial free energy $E_{\alpha\beta} \sim \Sigma_{\alpha\beta}R_{ne}^{2}$, which is, however, necessary in order to stabilize a narrow neck with finite radius $R_{ne} > 0$ as described by eqn (17).

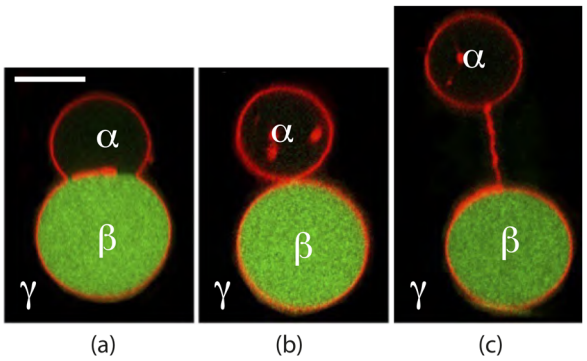

Fig. 15 (a) Giant vesicle membrane (red) enclosing a PEG-rich droplet α (black) and a dextran-rich droplet β (green). The vesicle is surrounded by the spectator phase γ (black); (b) osmotic deflation of the vesicle leads to the formation of a membrane neck that connects the spherical membrane segments around the α and β droplets; and (c) further deflation of the vesicle leads to the elongation of the membrane neck into a membrane nanotube between the two spherical membrane segments. The image in panel (b) is identical to the image in Fig. 6b. Scale bar in (a) is 25 μm and applies to all panels. Reused with permission from ref. 44, John Wiley and Sons, 2017.

11 Wetting geometries and contact angles

11.1 Apparent and intrinsic contact angles

The partial wetting morphologies as displayed in Fig. 3a and 4a involve apparent kinks along the contact line as observed for giant vesicles. In order to analyse these morphologies in a quantitative manner, we will now look at the contact angles between the surface of the droplet and the membrane of the vesicle. It is important to note that we need to distinguish between apparent contact angles on the scale of a few hundred nanometers as resolved by conventional light microscopy and intrinsic contact angles on the scale of a few tens of nanometers.

Using conventional light microscopy, one can observe three apparent contact angles with respect to the apparent membrane kink along the contact line. However, if such a kink persisted to nanoscopic length scales, the membrane would acquire a very large bending energy. Therefore, each apparent kink of the membrane shape should be replaced by a smoothly curved membrane segment on sufficiently small length scales.[55] Such smoothly curved segments have indeed been observed by stimulated emission depletion (STED) microscopy,[11] a super-resolution method, see Fig. 19 below. The smoothly curved membrane segments lead to the definition of two intrinsic contact angles, which replace the three apparent contact angles.

11.2 Apparent contact angles

The vesicle–droplet morphologies in Fig. 3a and 4a can be analyzed in terms of three apparent contact angles θ_{α}, θ_{β}, and θ_{γ}

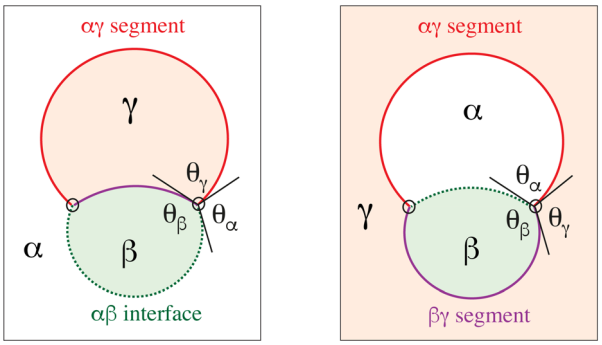

Fig. 16 Apparent contact angles θ_α, θ_β, and θ_γ for the vesicle–droplet systems in Fig. 3a and 4a: phase separation of (a) exterior solution and (b) interior solution into the two aqueous phases α and β. The contact angle θ_α is the angle between the αβ interface (dotted green line) and the αγ membrane segment (red line); the angle θ_β is the angle between the αβ interface and the βγ membrane segment (purple line); and θ_γ is the angle between the αγ and βγ membrane segments. In both (a) and (b), the contact lines, at which the three surface segments meet, are indicated by small black circles.

as depicted in Fig. 16. The contact angle θ_α is the angle between the αβ interface and the αγ membrane segment, the contact angle θ_β represents the angle between the αβ interface and the βγ segment, and the contact angle θ_γ is the angle between the βγ and the αγ membrane segments. More precisely, these angles are defined with respect to the tangent planes of these three surfaces at the contact line. The three apparent contact angles satisfy the obvious relation $\theta_\alpha + \theta_\beta + \theta_\gamma = 2\pi = 360^\circ$.

11.2.1 Force balance between surface tensions. Each of the three surfaces is subject to a certain mechanical tension as provided by the interfacial tension $\Sigma_{\alpha\beta}$ as well as by the mechanical tensions $\Sigma^{\mathrm{m}}_{\alpha\gamma}$ and $\Sigma^{\mathrm{m}}_{\beta\gamma}$ of the two membrane segments αγ and βγ. Note that the segment tensions have a superscript 'm' for 'membrane'. This distinction is necessary because the interfacial tension $\Sigma_{\alpha\beta}$ is a material parameter whereas the mechanical tensions of the membrane segments depend both on the size and shape of these segments.[4,19,58]

Mechanical equilibrium of the vesicle–droplet system implies that the interfacial tension $\Sigma_{\alpha\beta}$ has a constant value for the whole αβ interface. Likewise, the tensions $\Sigma^{\mathrm{m}}_{\alpha\gamma}$ and $\Sigma^{\mathrm{m}}_{\beta\gamma}$ are also constant everywhere on the αγ and βγ membrane segments. Furthermore, when the contact line does not move, the two segment tensions $\Sigma^{\mathrm{m}}_{\alpha\gamma}$ and $\Sigma^{\mathrm{m}}_{\beta\gamma}$ are balanced by the interfacial tension $\Sigma_{\alpha\beta}$. This force balance is illustrated in Fig. 17a for the case of partial wetting by a β droplet with $\theta_\beta < \theta_\alpha$.

The force balance in Fig. 17a implies that the three surface tensions form a triangle as shown in Fig. 17b.[4,5] Such a force balance is also possible in a liquid mixture with three coexisting liquid phases.[5,59] In the latter case, one β and one γ droplet may adhere to each other and coexist with the liquid bulk phase α which then leads to a force balance between the three interfacial tensions $\Sigma_{\alpha\beta}$, $\Sigma_{\beta\gamma}$, and $\Sigma_{\alpha\gamma}$ along the three-phase contact line.

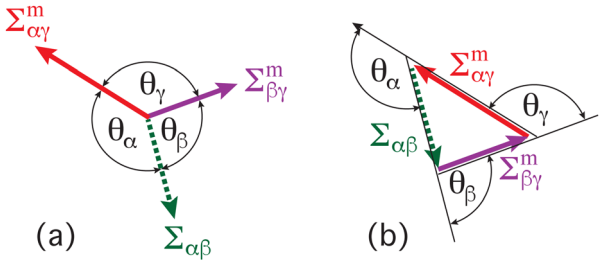

Fig. 17 Force balance between the interfacial tension $\Sigma_{\alpha\beta}$ (green) as well as the two membrane segment tensions $\Sigma^{\mathrm{m}}_{\beta\gamma}$ (purple), and $\Sigma^{\mathrm{m}}_{\alpha\gamma}$ (red) for partial wetting by the β droplet and $\theta_\beta < \theta_\alpha$: (a) each tension generates a force per unit length that pulls on the contact line in the direction of the corresponding arrow. The contact angles θ_α, θ_β, and θ_γ have been introduced in Fig. 16; and (b) in mechanical equilibrium, the three surface tensions must balance and form a triangle. The contact angles θ_i with i = α, β, and γ are the external angles of this triangle while the internal angles of the triangle are given by $\pi - \theta_i$.[4]

11.2.2 Segment tension difference. In general, each side of a triangle must be smaller than or equal to the sum of the two other sides. Applying this triangle inequality to the different sides of the tension triangle in Fig. 17b, a bit of algebra shows that the difference $\Sigma^{\mathrm{m}}_{\beta\gamma} - \Sigma^{\mathrm{m}}_{\alpha\gamma}$ of the two segment tensions satisfies the inequalities[6]

$$-\Sigma_{\alpha\beta} \le \Sigma^{\mathrm{m}}_{\beta\gamma} - \Sigma^{\mathrm{m}}_{\alpha\gamma} \le +\Sigma_{\alpha\beta}. \tag{18}$$

When the left hand inequality in eqn (18) becomes an equality, the resulting relation $\Sigma^{\mathrm{m}}_{\alpha\gamma} = \Sigma^{\mathrm{m}}_{\beta\gamma} + \Sigma_{\alpha\beta}$ describes complete wetting by the β phase with $\theta_\beta = 0$. Likewise, when the right hand inequality in eqn (18) becomes an equality, we obtain $\Sigma^{\mathrm{m}}_{\beta\gamma} = \Sigma^{\mathrm{m}}_{\alpha\gamma} + \Sigma_{\alpha\beta}$, corresponding to complete wetting by the α phase with $\theta_\alpha = 0$. Note that the tension difference $\Sigma^{\mathrm{m}}_{\alpha\gamma} - \Sigma^{\mathrm{m}}_{\beta\gamma} = -(\Sigma^{\mathrm{m}}_{\beta\gamma} - \Sigma^{\mathrm{m}}_{\alpha\gamma})$ satisfies the same inequalities, $-\Sigma_{\alpha\beta} \le \Sigma^{\mathrm{m}}_{\alpha\gamma} - \Sigma^{\mathrm{m}}_{\beta\gamma} \le +\Sigma_{\alpha\beta}$. Therefore, the positive interfacial tension $\Sigma_{\alpha\beta}$ and the negative value $-\Sigma_{\alpha\beta}$ of this tension provide upper and lower bounds for the difference of the two segment tensions.

11.3 Intrinsic contact angles

In Fig. 16, the shape contours of the vesicle membranes exhibit kinks at the contact lines between the αγ and βγ membrane segments. Such kinks are observed by conventional light microscopy of giant vesicles. However, if these kinks persisted to nanoscopic scales, the curvature radius of the shape contour would vanish and the membrane's bending energy would diverge.[55] To avoid such unphysical behavior, we require that the membrane has no kinks and is smoothly curved along the contact line on nanoscopic scales. This requirement reduces the three apparent contact angles to two intrinsic contact angles, θ^*_α and θ^*_β, as depicted in Fig. 18.

Inspection of this figure shows that the two intrinsic contact angles θ^*_α and θ^*_β now satisfy the relation

$$\theta^*_\alpha + \theta^*_\beta = \pi = 180^\circ \tag{19}$$

because the third contact angle $\theta_\gamma = \pi = 180^\circ$. In Fig. 18, the dashed black line represents the plane tangent to the

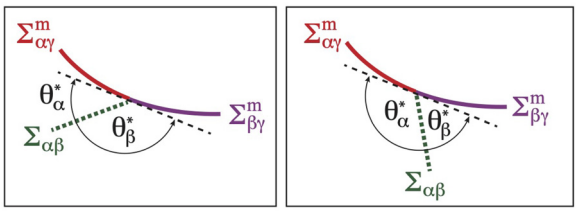

Fig. 18 Intrinsic contact angles θ_α^* and θ_β^* describing the force balance along the contact line for a smoothly curved membrane segment: (a) partial dewetting of the β droplet with $\theta_\alpha^* < \theta_\beta^*$. The limit of zero θ_α^* corresponds to complete wetting by the α phase and complete dewetting from the β phase; and (b) partial wetting by the β droplet with $\theta_\alpha^* > \theta_\beta^*$. The limit of zero θ_β^* corresponds to complete wetting by the β phase. The dashed black line represents the common tangent plane of the two membrane segments at the contact line. Same color code for the three surface segments and tensions as in Fig. 17.

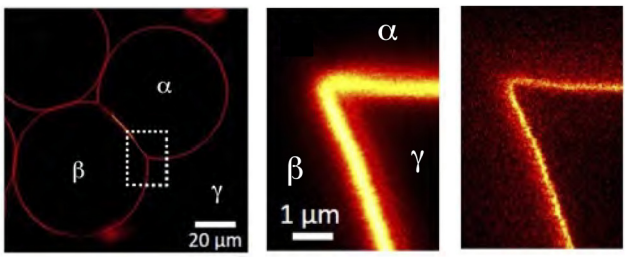

Fig. 19 Apparent membrane kinks are low-resolution images of highly curved membrane segments: (a) GUV with an interior compartment that contains a PEG-rich α droplet and a dextran-rich β droplet. The region enframed by the white-dashed rectangle contains one membrane kink which is enlarged in panels (b) and (c); and (b) and (c) the highly curved membrane segment cannot be resolved by confocal microscopy as in (b) but by STED as in (c), which leads to about 220 nm for the curvature radius.[11]

membrane at the contact line. More precisely, this plane represents the common tangent to both membrane segments αγ and βγ at the contact line. Therefore, the term "smoothly curved" as used here implies that both membrane segments have the same tangent plane at the contact line as observed by STED microscopy,[11] see Fig. 19.

11.3.1 Force balance for smoothly curved membranes. Projecting the three surface tensions in Fig. 18 onto the common tangent plane at the contact line, we obtain the segment tension difference

$$\Sigma^{\mathrm{m}}_{\beta\gamma} - \Sigma^{\mathrm{m}}_{\alpha\gamma} = +\Sigma_{\alpha\beta}\cos\theta_\alpha^* = -\Sigma_{\alpha\beta}\cos\theta_\beta^* \qquad (20)$$

where the second equality follows from $\theta_\beta^* = \pi - \theta_\alpha^*$. Because $-1 \le \cos\theta_\alpha^* \le +1$, the segment tension difference as given by eqn (20) again satisfies the inequalities in eqn (18). One should also note that the tangential force balance in eqn (20) does not involve any curvature-elastic parameter such as the bending rigidity or the spontaneous curvature. For sufficiently short contact lines, the tangential force balance in eqn (20) involves another term, which is proportional to the contact line tension λ_{cl}, see eqn (S6) in Section S6 (ESI†).

11.4 Consequences of force balance between tensions

The force balance of the interfacial tension $\Sigma_{\alpha\beta}$ with the two membrane segment tensions $\Sigma^{\mathrm{m}}_{\beta\gamma}$, and $\Sigma^{\mathrm{m}}_{\alpha\gamma}$ as described by Fig. 17 and 18 has some important consequences.

11.4.1 Positive mechanical tensions of membrane segments. The interfacial tension $\Sigma_{\alpha\beta}$ is always positive as required by thermodynamic stability. In principle, the mechanical tensions $\Sigma^{\mathrm{m}}_{\alpha\gamma}$ and $\Sigma^{\mathrm{m}}_{\beta\gamma}$ of the two membrane segments αγ and βγ can be positive or negative, corresponding to stretched or compressed segments.[19] However, force balance as in Fig. 17 is not possible if one segment tension is positive and the other segment tension is negative. Furthermore, two negative segment tensions would necessarily imply a contact angle $\theta_\gamma > \pi = 180^\circ$ whereas all experimental data are consistent with $\theta_\gamma \le \pi = 180^\circ$.

One large set of data for the measured values of the apparent contact angles is provided in Fig. 20 where all three apparent contact angles are displayed for 63 individual vesicles with adhering droplets. These contact angles are plotted as functions of the volume-to-area ratio $\bar{v} \equiv 6\sqrt{\pi}V/A^{3/2}$, defined in terms of vesicle volume V and membrane area A. The parameter $\bar{v}$ satisfies $\bar{v} \le 1$ for all vesicle shapes and attains its largest value $\bar{v} = 1$ for spherical vesicles as follows from the isoperimetric inequality.[41,42] Inspection of Fig. 20 shows that the contact angle θ_γ always satisfies $\theta_\gamma \le \pi = 180^\circ$, which implies that

$$\Sigma^{\mathrm{m}}_{\alpha\gamma} \ge 0 \quad \text{and} \quad \Sigma^{\mathrm{m}}_{\beta\gamma} \ge 0. \qquad (21)$$

A membrane segment with mechanical membrane tension close to zero exhibits finger-like protrusions as displayed in Fig. 25 below.

11.4.2 Surface tensions and apparent contact angles. For any triangle, the law of sines implies that the ratio of any two

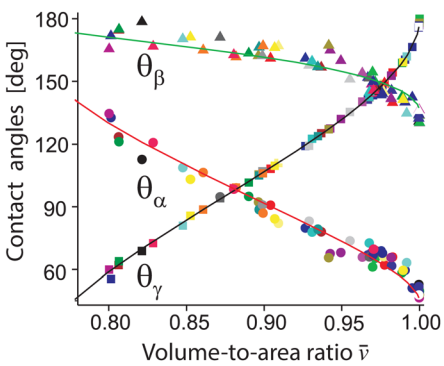

Fig. 20 Apparent contact angles θ_α, θ_β, and θ_γ as measured by phase contrast microscopy for 63 individual vesicles, indicated by different colors.[55] Each of these vesicles enclosed one PEG-rich α droplet and one dextran-rich β droplet. The three contact angles are plotted as functions of the volume-to-area ratio $\bar{v}$ of the vesicles. For a vesicle with volume V and membrane area A, the shape parameter $\bar{v} \equiv 6\sqrt{\pi}V/A^{3/2} \le 1$.

sides of the triangle is equal to the ratio of the sines of the two internal angles that are opposite to these two sides. Applying this law of sines to the tension triangle in Fig. 17b, we obtain the equalities

$$\frac{\Sigma^{\mathrm{m}}_{\alpha\gamma}}{\Sigma_{\alpha\beta}} = \frac{\sin\theta_\beta}{\sin\theta_\gamma} \quad \text{and} \quad \frac{\Sigma^{\mathrm{m}}_{\beta\gamma}}{\Sigma_{\alpha\beta}} = \frac{\sin\theta_\alpha}{\sin\theta_\gamma}. \tag{22}$$

By taking the ratio of these two equations, we also obtain the relation $\Sigma^{\mathrm{m}}_{\alpha\gamma}/\Sigma^{\mathrm{m}}_{\beta\gamma} = \sin\theta_\beta/\sin\theta_\alpha$. Therefore, all ratios between two of the three surface tensions $\Sigma_{\alpha\beta}$, $\Sigma^{\mathrm{m}}_{\alpha\gamma}$, and $\Sigma^{\mathrm{m}}_{\beta\gamma}$ can be expressed in terms of the apparent contact angles θ_α, θ_β, and θ_γ.

11.5 Complete wetting near critical demixing points

Next, let us consider a situation, in which the membrane prefers the β phase over the α phase, leading to partial wetting of the membrane by the β phase for some tie line away from the critical demixing point. As we move closer to this critical point, the interfacial tension $\Sigma_{\alpha\beta}$ goes continuously to zero as in Fig. S4 (ESI†) whereas the membrane segment tensions $\Sigma^{\mathrm{m}}_{\alpha\gamma}$ and $\Sigma^{\mathrm{m}}_{\beta\gamma}$ will attain the same finite value Σ^*, because the two phases α and β become identical at the critical point. As a consequence, the tension difference between the two membrane segments, as given by

$$\Sigma^{\mathrm{m}}_{\alpha\gamma} - \Sigma^{\mathrm{m}}_{\beta\gamma} = \Sigma^{\mathrm{m}}_{\alpha\gamma} - \Sigma^* - (\Sigma^{\mathrm{m}}_{\beta\gamma} - \Sigma^*), \tag{23}$$

also vanishes at the critical point. We now assume, as in the theory of liquid–liquid wetting in the absence of membranes,[59–61] that the tension difference $\Sigma^{\mathrm{m}}_{\alpha\gamma} - \Sigma^{\mathrm{m}}_{\beta\gamma}$ vanishes more slowly than the interfacial tension as we approach the critical point. It then follows that the tension difference $\Sigma^{\mathrm{m}}_{\alpha\gamma} - \Sigma^{\mathrm{m}}_{\beta\gamma}$ becomes equal to the interfacial tension $\Sigma_{\alpha\beta}$ at a certain tie line, which has a finite distance from the critical point. Therefore, this tie line is characterized by

$$\Sigma^{\mathrm{m}}_{\alpha\gamma} - \Sigma^{\mathrm{m}}_{\beta\gamma} = \Sigma_{\alpha\beta} \quad \text{(onset of complete wetting)}, \tag{24}$$

which implies that the vesicle–droplet system undergoes a transition from partial to complete wetting as one approaches the critical demixing point. This behavior has been demonstrated experimentally for (i) aqueous PEG–dextran solutions, which undergo segregative phase separation, see the schematic phase diagram in Fig. S5 (ESI†) and the nanotube patterns in Fig. 10, as well as for (ii) aqueous solutions of the soybean protein glycinin and sodium chloride, see the phase diagram in Fig. 1 and the vesicle–droplet morphologies in Fig. 22 below.

11.6 Affinity contrast between coexisting liquid phases

The segment tension difference as given by eqn (18) and (20) plays an important role in the theory. Furthermore, as explained in Section S9 (ESI†), this segment tension difference can be interpreted as the affinity contrast between the two coexisting aqueous phases α and β. Therefore, we now define the affinity contrast $W_{\beta\alpha}$ *via*[5]

$$W_{\beta\alpha} \equiv \Sigma^{\mathrm{m}}_{\beta\gamma} - \Sigma^{\mathrm{m}}_{\alpha\gamma} = -W_{\alpha\beta}, \tag{25}$$

which is negative if the membrane prefers the β over the α phase and positive if the membrane prefers the α over the β phase. The magnitude and sign of the affinity contrast depends on the underlying molecular interactions between the membrane and the aqueous phases.

11.6.1 Rescaled affinity contrast. It is also useful to consider the rescaled affinity contrast

$$w_{\beta\alpha} \equiv \frac{W_{\beta\alpha}}{\Sigma_{\alpha\beta}} = \frac{\Sigma^{\mathrm{m}}_{\beta\gamma} - \Sigma^{\mathrm{m}}_{\alpha\gamma}}{\Sigma_{\alpha\beta}}, \tag{26}$$

which depends on the rescaled segment tensions $\Sigma^{\mathrm{m}}_{\beta\gamma}/\Sigma_{\alpha\beta}$ and $\Sigma^{\mathrm{m}}_{\alpha\gamma}/\Sigma_{\alpha\beta}$ of the two membrane segments. The inequalities for the difference of the segment tensions in eqn (18) imply that the rescaled affinity contrast $w_{\beta\alpha}$ satisfies the inequalities

$$-1 \le w_{\beta\alpha} \le +1 \tag{27}$$

where $w_{\beta\alpha} = -1$ corresponds to complete wetting by the β phase and $w_{\beta\alpha} = +1$ describes complete wetting by the α phase. The range of $w_{\beta\alpha}$ values as given by eqn (27) defines the force balance regime, which can be visualized within the two-dimensional parameter space defined by the rescaled segment tensions $x \equiv \Sigma^{\mathrm{m}}_{\beta\gamma}/\Sigma_{\alpha\beta}$ and $y \equiv \Sigma^{\mathrm{m}}_{\alpha\gamma}/\Sigma_{\alpha\gamma}$, as shown in Fig. 21.

11.6.2 Force balance regime. Inspection of the force balance regime in Fig. 21 shows that this regime is located within three boundary lines. The boundary line CWα corresponds to complete wetting by the α phase while the boundary line CWβ represents complete wetting by the β phase. In terms of the coordinates $x = \Sigma^{\mathrm{m}}_{\beta\gamma}/\Sigma_{\alpha\beta}$ and $y = \Sigma^{\mathrm{m}}_{\alpha\gamma}/\Sigma_{\alpha\beta}$ used in Fig. 21, the third

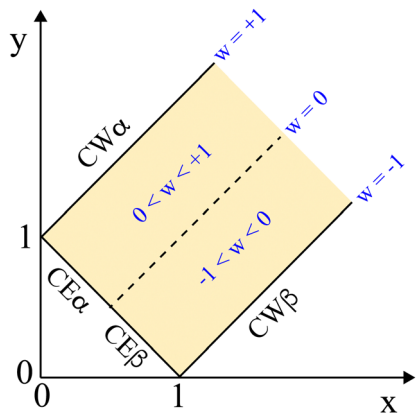

Fig. 21 Force balance regime (yellow) within the two-dimensional parameter space defined by $x = \Sigma^{\mathrm{m}}_{\beta\gamma}/\Sigma_{\alpha\beta}$ and $y = \Sigma^{\mathrm{m}}_{\alpha\gamma}/\Sigma_{\alpha\beta}$, corresponding to the membrane segment tensions $\Sigma^{\mathrm{m}}_{\alpha\gamma}$ and $\Sigma^{\mathrm{m}}_{\beta\gamma}$ rescaled by the interfacial tension $\Sigma_{\alpha\beta}$. Within the yellow regime, the three surface tensions can balance each other along the contact line of droplet and vesicle. The force balance regime is bounded from below by the CWβ line of complete wetting of the vesicle membrane by the β phase with $w \equiv w_{\beta\alpha} = -1$ and from above by the CWα line of complete wetting by the α phase with $w = +1$. The left boundary with $y = 1 - x$ corresponds to complete engulfment of an α droplet (CEα) and to complete engulfment of a β droplet (CEβ), depending on the sign of the affinity contrast w. Balanced adhesion with $w = 0$ (dashed line) divides the force balance regime up into a partial wetting regime by the β phase with $-1 < w < 0$ and a partial wetting regime by the α phase with $0 < w < +1$.

boundary line is given by[6]

$$y = \frac{\Sigma^{\mathrm{m}}_{\beta\gamma}}{\Sigma_{\alpha\beta}} = 1 - \frac{\Sigma^{\mathrm{m}}_{\alpha\gamma}}{\Sigma_{\alpha\beta}} = 1 - x, \tag{28}$$

which truncates the force balance regime for small values of x and y. The relation between x and y as given by eqn (28) is equivalent to the tension relation $\Sigma_{\alpha\beta} = \Sigma^{\mathrm{m}}_{\alpha\gamma} + \Sigma^{\mathrm{m}}_{\beta\gamma}$, which implies the apparent contact angle $\theta_\gamma = 0$ as follows from the tension triangle in Fig. 17b.

Without the membrane, the relation in eqn (28) would describe complete wetting by the γ phase which is, however, not possible in the presence of the membrane. In the latter case, the relation in eqn (28), which is equivalent to $\theta_\gamma = 0$, corresponds to complete engulfment of a condensate droplet by the vesicle membrane. This droplet may be formed by the α or by the β phase, depending on the sign of the affinity contrast $w_{\beta\alpha}$ as indicated by the lettering CEα and CEβ in Fig. 21.

11.6.3 Affinity contrast in terms of apparent contact angles. When we combine the definition of the rescaled affinity contrast $w_{\beta\alpha}$ in eqn (26) with the equalities in eqn (22), we obtain the relationship

$$w_{\beta\alpha} = \frac{\Sigma^{\mathrm{m}}_{\beta\gamma} - \Sigma^{\mathrm{m}}_{\alpha\gamma}}{\Sigma_{\alpha\beta}} = \frac{\sin\theta_\alpha - \sin\theta_\beta}{\sin\theta_\gamma} \tag{29}$$

between the rescaled affinity contrast $w_{\beta\alpha}$ and the apparent contact angles. The affinity contrast $W_{\beta\alpha}$ is then given by $W_{\beta\alpha} = w_{\beta\alpha}\Sigma_{\alpha\beta}$, where the interfacial tension $\Sigma_{\alpha\beta}$ represents another material parameter that can be measured, see the experimental data for the interfacial tension for PEG–dextran solutions in Fig. S4 (ESI†).

The relationship in eqn (29) is quite remarkable because the affinity contrast is a mechanical quantity whereas the apparent contact angles are purely geometric quantities, which can be directly measured by light microscopy as in Fig. 20. Therefore, the relationship in eqn (29) can be used to deduce the affinity contrast from the measured values of the apparent contact angles. One example for this deduction is shown in Fig. 22b where the rescaled affinity contrast $w_{\beta\alpha}$ is plotted as a function of NaCl concentration for fixed glycinin concentration in aqueous solutions of glycinin and NaCl.

11.6.4 Affinity contrast in terms of intrinsic contact angles. Using the definition of the rescaled affinity contrast $w_{\beta\alpha}$ in eqn (26) together with the tangential force balance in terms of the intrinsic contact angles as given by eqn (20), we also obtain the relation

$$w_{\beta\alpha} = \frac{\Sigma^{\mathrm{m}}_{\beta\gamma} - \Sigma^{\mathrm{m}}_{\alpha\gamma}}{\Sigma_{\alpha\beta}} = \cos\theta^*_\alpha = -\cos\theta^*_\beta \tag{30}$$

between the rescaled affinity contrast $w_{\beta\alpha}$ and the intrinsic contact angles θ^*_α and θ^*_β. Thus, the force balance regime in Fig. 21, which has been derived from the tension triangle in Fig. 17 in terms of the three apparent contact angles θ_α, θ_β, and θ_γ, also applies to the force balance in Fig. 18, which depends on the two intrinsic contact angles θ^*_α and θ^*_β.

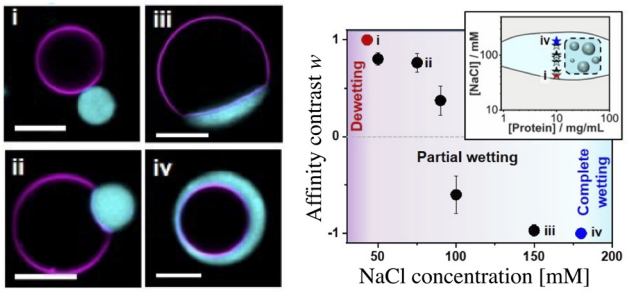

(a) (b)

Fig. 22 GUV membranes (magenta) interacting with exterior condensate droplets (cyan), enriched in the soybean protein glycinin:[12] (a) four vesicle–droplet morphologies, labeled by (i)–(iv), corresponding to four solution conditions as specified in the inset of (b). Panel (i) displays complete dewetting of the droplet from the membrane whereas panel (iv) represents complete wetting of the membrane by the droplet; and (b) rescaled affinity contrast $w \equiv w_{\beta\alpha}$ as defined by eqn (26) and determined from the apparent contact angles. The variation of the affinity contrast is shown as a function of the NaCl concentration for fixed protein concentration, see inset with the phase diagram *versus* protein and NaCl concentrations. The affinity contrast varies from $w = -1$ for complete wetting by the glycinin-rich droplet, labeled by (iv), to $w = +1$ for complete dewetting from this droplet, labeled by (i). The inset in (b) represents a reduced version of Fig. 1.

11.6.5 Relation between apparent and intrinsic contact angles. Because the rescaled affinity contrast $w_{\beta\alpha}$ can be expressed both in terms of the apparent contact angles by eqn (29) and in terms of the intrinsic contact angles by eqn (30), we obtain the explicit relationship

$$\cos\theta^*_\alpha = -\cos\theta^*_\beta = \frac{\sin\theta_\alpha - \sin\theta_\beta}{\sin\theta_\gamma} \tag{31}$$

between the apparent and intrinsic contact angles. Note that eqn (31) is a purely geometric relationship that does not involve any curvature-elastic parameters. This relationship was originally derived using the assumption that the two membrane segments $\alpha\gamma$ and $\beta\gamma$ have the same curvature-elastic parameters.[55] The derivation of eqn (31) as given here shows that this relation follows directly from the much weaker assumption that the membrane is smoothly curved close to the contact line as in Fig. 18, which has been experimentally confirmed by the STED measurements in Fig. 19c.

11.6.6 Affinity contrast for aqueous glycinin solutions. Aqueous solutions of the soybean protein glycinin and NaCl undergo phase separation into a protein-rich and a protein-poor phase, see the corresponding phase diagram in Fig. 1. When the coexistence region of these two phases is crossed by changing the NaCl concentration for fixed protein concentration, as in the inset of Fig. 22b, one observes the sequence of vesicle–droplet morphologies displayed in Fig. 22a. Panel (i) of this sequence corresponds to complete dewetting of the glycinin-rich phase from the vesicle membrane, which is equivalent to complete wetting of the vesicle by the glycinin-poor phase. On the other hand, panel iv in Fig. 22a displays complete wetting of the vesicle by the glycinin-rich phase and complete dewetting from the glycinin-poor phase.

Thus, changing the salt concentration as in the inset of Fig. 22b, the vesicle–droplet morphologies change in a continuous manner from complete wetting of the vesicle membrane to complete dewetting from the membrane by the exterior glycinin-rich droplet, corresponding to the β phase. Note that the phase diagram for aqueous solutions of glycinin and NaCl exhibits an upper and a lower critical point, located at the upper and lower binodal of the phase diagram in Fig. 1. Thus, complete wetting by glycinin-rich β droplets takes place close to the upper critical point whereas complete wetting by the glycinin-poor phase α is observed close to the lower critical point.

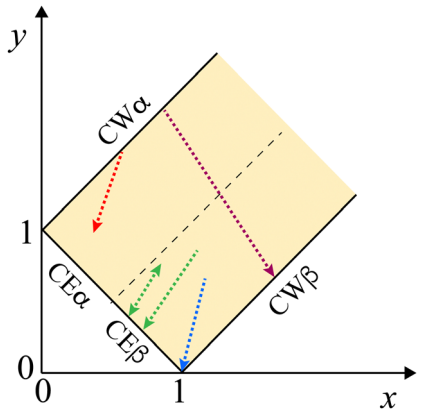

Fig. 23 Morphological pathways of vesicle–droplet systems within the two-dimensional parameter space defined by the rescaled segment tensions $x = \Sigma^{m}_{\alpha\gamma}/\Sigma_{\alpha\beta}$ and $y = \Sigma^{m}_{\beta\gamma}/\Sigma_{\alpha\beta}$. Along the red pathway, the vesicle–droplet system starts from complete wetting of the vesicle membrane by the α phase and then undergoes a complete-to-partial wetting transition as in Fig. 10. The purple pathway starts from complete wetting by the glycinin-poor α phase and ends up with complete wetting by the glycinin-rich β phase as in Fig. 22. The green pathway starts from partial wetting of the vesicle membrane by the β droplet, leading to partial engulfment of this droplet, and ends up with the complete engulfment of the droplet as in Fig. 6a. The green pathway with two arrowheads describes the reversible transformation between partial and complete engulfment of the β droplet, which can be controlled by light as in Fig. 24. Finally, the blue pathway reaches the corner point with $x = 1$ and $y = 0$, corresponding to ultralow segment tension $\Sigma^{m}_{\beta\gamma}$, which leads to fingering of the βγ segment as in Fig. 25.

12 Transitions of vesicle–droplet morphologies

12.1 Complete to partial wetting transitions

The segregative phase diagram for aqueous PEG–dextran solutions exhibits one critical demixing point at low concentrations of the two polymers (Fig. S1 and S5, ESI†). Starting from the one-phase region below the binodal line and crossing this line by increasing the polymer concentrations inside the vesicle *via* osmotic deflation, one first observes complete wetting as in Fig. 10a and Fig. S5b (ESI†). When the interior polymer concentrations is further increased, the vesicle–droplet systems exhibit partial wetting as in Fig. 10b and Fig. S5c (ESI†).

Therefore, aqueous PEG–dextran solutions lead to complete wetting of the vesicle membranes close to the critical point and to a transition from complete to partial wetting further away from this point,[10] in accordance with the theoretical analysis in Section 11.5. This morphological pathway corresponds to the red line in the force balance regime of Fig. 23.

12.2 From complete dewetting to complete wetting

Another morphological pathway is displayed in Fig. 22a. By varying the NaCl concentration as in the inset of Fig. 22b, one crosses the associative phase diagram of aqueous glycinin–NaCl solutions, by starting from relatively low NaCl concentrations close to the lower binodal and ending up with relatively high NaCl concentrations close to the upper binodal of the phase diagram.

Along this pathway, one observes complete dewetting of the vesicle membrane from the glycinin-rich phase as in panel (i) of Fig. 22a close to the lower binodal but complete wetting by the glycinin-rich phase close to the upper binodal as displayed in panel iv of Fig. 22a. This salt-induced morphological pathway corresponds to the purple line in Fig. 23, which crosses the whole force balance regime.

12.3 Light-induced engulfment of condensate droplets

The surface area of vesicle membranes containing lipids with an azobenzene group can be changed in a fast and reversible manner using light of different wavelengths.[39,40] The azo-lipids attain two molecular conformations, *trans* and *cis*, which can be transformed into each other by illumination with light of different wavelengths. The *cis*-state has a larger area per lipid which implies that the conformational change from *trans* to *cis* increases the membrane area of the vesicle, which has been recently used to switch the vesicle–droplet systems between partial and complete engulfment, see Fig. 24. In this example, an azo-PC lipid was used that transforms from *trans* to *cis* under illumination with UV light and from *cis* to *trans* under blue light.

An increase in membrane area reduces the segment tensions $\Sigma^{m}_{\alpha\gamma}$ and $\Sigma^{m}_{\beta\gamma}$ whereas a decrease in the membrane area increases these tensions. Thus, the reversible transformation between partial and complete engulfment provides an example for the green pathway with two arrowheads in Fig. 23.

12.4 Tensionless membrane segments

For vesicles exposed to glycinin-rich β droplets, unusual vesicle–droplet morphologies have also been observed, in which the βγ membrane segments in contact with these droplets develop fingering protrusions as displayed in Fig. 25.[12] These morphologies are formed along the blue morphological pathway in Fig. 23, which approaches the corner point of the force balance regime with $x = 1$ and $y = 0$, corresponding to a tensionless βγ membrane segment.

12.5 Measurements of intrinsic contact angles

The intrinsic contact angle θ^{*}_{α} has been directly measured using STED microscopy.[11] In contrast to conventional confocal

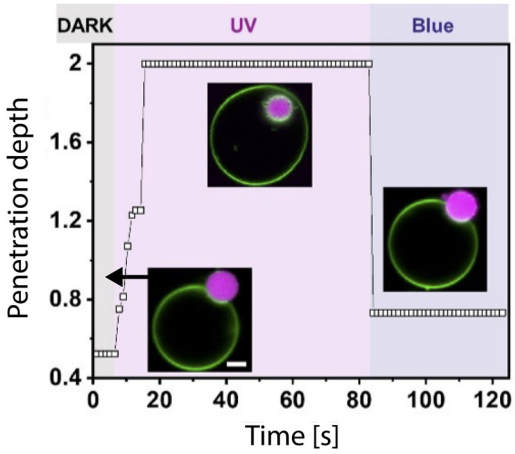

Fig. 24 Light-induced engulfment of exterior glycinin-rich condensate droplet (magenta) by vesicle membrane (green) that contains azo-lipids.[13] Initially, the vesicle–droplet system is in the dark, the azo-lipids are in their *trans* conformations, and the droplet is partially engulfed. When illuminated with UV light, the azo-lipids are transformed into their *cis* conformations, the membrane area increases, and the droplet becomes completely engulfed within about 9 s. When illuminated by blue light after 83 s, the azo-lipids are transformed back to their *trans* conformations and the membrane area decreases, which leads back to partial engulfment within less than 650 μs. The penetration depth is a purely geometric quantity, varying from 0 for dewetting to 2 for complete engulfment.

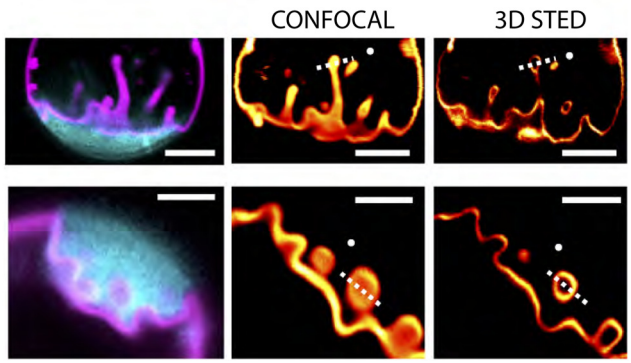

Fig. 25 Fingering protrusions of βγ membrane segments, which are in contact with glycinin-rich condensate droplets (cyan), denoted by β. Scale bars: 5 μm.[12] These segments are under ultralow mechanical tension which favors the transfer of membrane area from the αγ to the βγ segments. Within the force balance regime in Fig. 23, these vesicle–droplet morphologies are formed when the blue morphological pathway approaches the corner point with $x = 1$ and $y = 0$, at which the membrane segment tension $\Sigma^{m}_{\beta\gamma}$ vanishes.

microscopy, STED is able to resolve the smoothly curved membrane segments αγ and βγ, see Fig. 19c, as well as the intrinsic contact angles θ^*_α and $\theta^*_\beta = \pi - \theta^*_\alpha$ between these segments and the αβ interface. The STED values for the intrinsic contact angle θ^*_α are displayed in Fig. S11a (ESI†).

Furthermore, the relationship between the intrinsic and the apparent contact angles as given by eqn (31) can be used to determine the intrinsic contact angles from the measured values of the apparent contact angles.[55] Thus, inserting the measured values of the apparent contact angles as displayed in Fig. 20 into eqn (31), one obtains the estimate $\cos\theta^*_\alpha = 0.714 \pm 0.075$ which implies the nearly constant value $\theta^*_\alpha \simeq 44^\circ \simeq \pi/4$ for all values of the volume-to-area ratio $\bar{v}$ as displayed in Fig. S11b (ESI†).

12.6 Important aspects of intrinsic contact angles

The intrinsic contact angles are difficult to measure but become important whenever the geometry of the vesicle–droplet systems involves membrane or interface segments with nanoscopic dimensions. Examples for such systems are provided (i) by the closure of membrane necks during complete engulfment as in Fig. 14, (ii) by nanotubes adhering to the αβ interface as displayed in Fig. 26, and (iii) by the nucleation of condensate droplets at vesicle membranes.[45,46]

12.6.1 Nanotubes adhering to αβ interface. For nanotubes adhering to an αβ interface as in Fig. 9 and 26, the intrinsic contact angle determines how far these adhering nanotubes "sink into" the αβ interface and, thus, determines the area ratio $A_{\alpha\gamma}/A_{\beta\gamma}$ of the αγ and βγ tube segments.

13 Transitions between nanotubes and nanosheets

13.1 From nanotubes to nanosheets

When the nanotubes adhere to the αβ interface, the competition between the membrane's bending energy and the adhesion free energy leads to a fascinating shape transformation from adhering nanotubes to adhering double-membrane sheets or "pancakes" as experimentally observed for interior

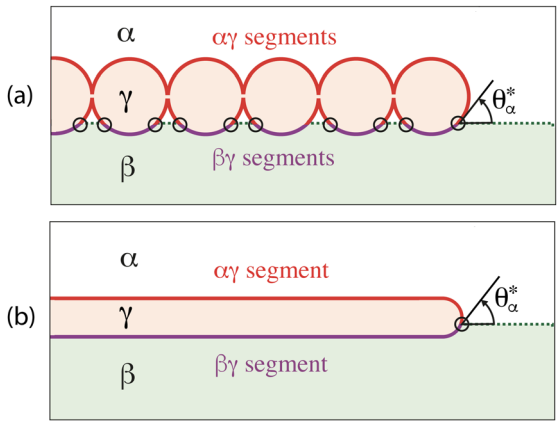

Fig. 26 Side views of membrane nanotubes (red/purple) adhering to a weakly curved αβ interface (dotted green) for partial wetting of the membrane by the two liquid phases α and β. The αβ interface forms the intrinsic contact angle θ^*_α with the αγ membrane segment of the tubes: (a) multispherical tube consisting of equally sized spheres, which are connected by closed membrane necks and filled with γ phase (pink). Each sphere consists of one αγ membrane segment (red) in contact with the α phase and one βγ segment (purple) exposed to the β phase; and (b) cylindrical tube which is closed by a spherical endcap, filled with γ phase, and divided up into one αγ (red) and one βγ (purple) segment. In both (a) and (b), the contact line is indicated by small black circles.

phase separation of PEG–dextran solutions, see the example in Fig. 27.[15]

13.2 From nanosheets to nanotubes

For interior PEG–dextran solutions, the reverse transformation from adhering double-membrane sheets to nanotubes has also been observed. One example is displayed in Fig. 28. One important control parameter for both the tube-to-sheet transformation in Fig. 27 and the sheet-to-tube transformation in Fig. 28 is the interfacial tension $\Sigma_{\alpha\beta}$ as explained in the next paragraphs.

13.3 Bistable free energy landscape

The optical microscopy images in Fig. 27 and 28 provide direct evidence for the presence of both nanotubes and nanosheets for the same vesicle–droplet system. As a consequence, these systems possess a bistable free energy landscape, with two local minima corresponding to tubes and sheets. Such a free energy landscape has been obtained by a systematic shape analysis of the tubes and sheets. The double-membrane sheets are approximately axisymmetric, which implies that the two-dimensional shape of such a sheet is determined by its cross-section, see the STED microscopy image in Fig. 29. The theoretical analysis fitted this cross-section to piece-wise circular segments for different values for the spontaneous curvatures $m_{\alpha\gamma}$ and $m_{\beta\gamma}$.[15]

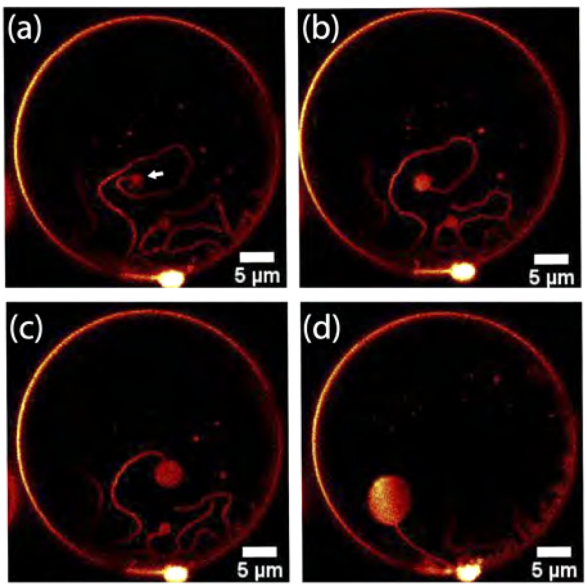

Fig. 27 Transformation of a single nanotube into a double-membrane sheet, both adhering to the αβ interface between the PEG-rich phase α and the dextran-rich phase β; top view from the α phase onto the αβ interface: (a) the tube-to-sheet transformation starts from the interior end of the nanotube, which then forms a small sheet (white arrow); (b) and (c) the sheet grows continuously, thereby shortening the tube; and (d) eventually, the growing sheet comes close to the other tube end at the membrane of the mother vesicle. This tube-to-sheet transformation takes about 11 seconds. From Movie S2 of ref. 15.

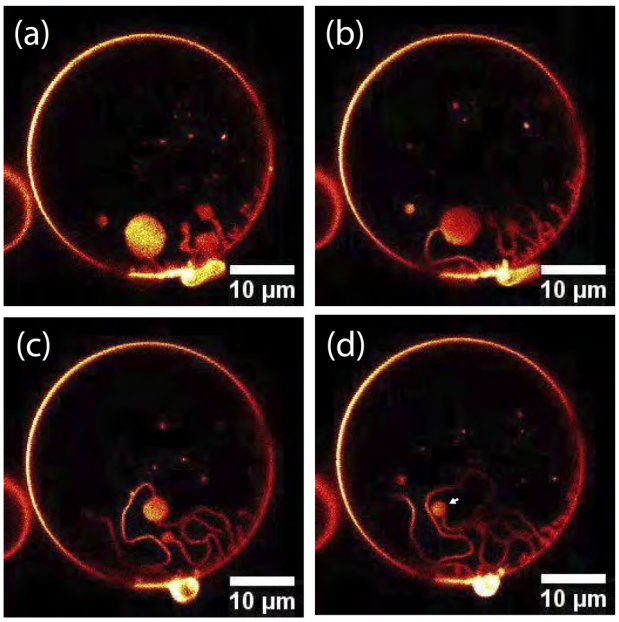

Fig. 28 Transformation of a single double-membrane sheet into a nanotube for the same vesicle–droplet system as in Fig. 27: (a) the sheet-to-tube transformation starts from a sheet close to the membrane of the mother vesicle; (b)–(d) the sheet shrinks and the tube segment between the sheet and the mother vesicle grows continuously until the membrane area of the sheet has been transformed into a long tube. The complete transformation process from sheet to tube takes about 150 seconds. From Movie S4 of ref. 15.

13.4 Simplified sheet geometry

Additional insight into the tube-to-sheet and sheet-to-tube transformations as displayed in Fig. 27 and 28 can be obtained by simplifying the sheet geometry in Fig. 29 to a double-membrane disk as depicted in Fig. 30. This simplification is motivated by the very anisotropic shape of the double-membrane sheet, which has a lateral extension of the order of ten micrometers but a thickness below a few hundred nanometers as in Fig. 29.[15] This separation of length scales

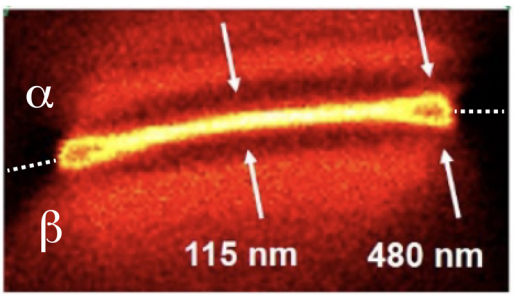

Fig. 29 Cross-section of double-membrane sheet (yellow) as observed by STED microscopy.[15] The PEG-rich α phase is above, the dextran-rich β phase below this sheet. These two phases are separated by the αβ interface, which is located along the white dashed line segments. The cross-section consists of two weakly-curved faces with a separation of 115 nm and of a highly-curved rim. Close to the rim, the two faces bulge away from each other with a maximal separation of 480 nm. The lateral extension of the sheet is 10 μm.

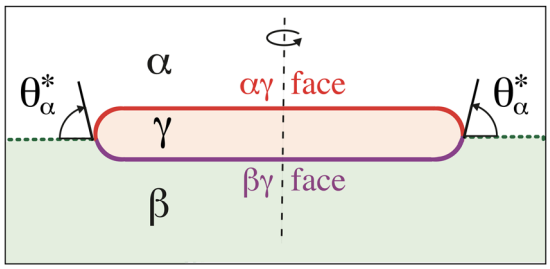

Fig. 30 Double-membrane disk at a weakly curved αβ interface (green dotted line): the disk provides a simplified geometry for the double-membrane sheet as displayed in Fig. 29. This geometry captures the basic separation of length scales between the two weakly curved faces, consisting of αγ (red) and βγ (purple) membrane segments, and the highly curved rim of the sheet. The disk is taken to be axisymmetric with respect to the vertical dashed line. The angle between the αβ interface and the αγ membrane segment is equal to the intrinsic contact angle θ^*_α.

can be encoded in the double-membrane disk. Indeed, both the double-membrane sheet and the double-membrane disk exhibit two weakly curved and parallel faces, which are connected by a highly curved rim. One face is provided by the αγ membrane segment in contact with the α phase, the other face by the βγ membrane segment exposed to the β phase.

The membrane area of the two faces is much larger than the membrane area of the rim which implies that the free energies of both sheet and disk are dominated by the free energy of the two faces. If we denote the membrane area of the two faces by $A^{\rm fac}_{\alpha\gamma}$ and $A^{\rm fac}_{\beta\gamma}$ $\simeq A^{\rm fac}_{\alpha\gamma}$, the negative adhesion free energy of the sheets is proportional to $A^{\rm fac}_{\alpha\gamma}\Sigma_{\alpha\beta}$ with interfacial tension $\Sigma_{\alpha\beta}$.[10,15] The bending energy of the two faces is given by

$$\sigma_{\alpha\gamma}A^{\rm fac}_{\alpha\gamma} + \sigma_{\beta\gamma}A^{\rm fac}_{\beta\gamma} \simeq (\sigma_{\alpha\gamma} + \sigma_{\beta\gamma})A^{\rm fac}_{\alpha\gamma} \qquad (32)$$

with the curvature-elastic tensions $\sigma_{\alpha\gamma}$ and $\sigma_{\beta\gamma}$ of the weakly curved αγ and βγ faces. The adhesion free energy proportional to the interfacial tension $\Sigma_{\alpha\beta}$ favors double-membrane sheets whereas large curvature-elastic tensions of the two faces act to suppress the formation of such sheets. Therefore, the nanotube transforms into a double-membrane sheet for

$$\Sigma_{\alpha\beta} \gg \sigma_{\alpha\gamma} + \sigma_{\beta\gamma} \quad \text{(tube-to-sheet)} \qquad (33)$$

whereas the sheet transforms into a nanotube for

$$\Sigma_{\alpha\beta} \ll \sigma_{\alpha\gamma} + \sigma_{\beta\gamma} \quad \text{(sheet-to-tube).} \qquad (34)$$

The inequalities in eqn (33) and (34) provide sufficient conditions for the two morphological transformations and identify two distinct parameter regimes of the bistable free energy landscape. Therefore, changes in the interfacial tension $\Sigma_{\alpha\beta}$ of the PEG–dextran solutions (Fig. S4, ESI†) can be used to induce both the tube-to-sheet and the sheet-to-tube transformations.

13.5 Dense layers of adhering nanotubes

Membrane nanotubes provide a very efficient mechanism to store excess membrane area when the vesicle membrane has a large spontaneous curvature. Indeed, the nanotubes can adapt

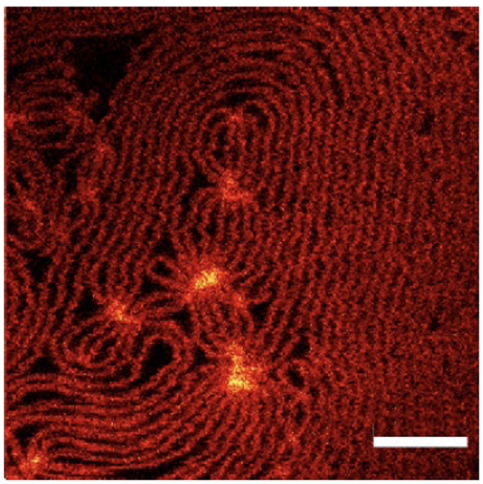

Fig. 31 Dense layer of membrane nanotubes (red) adhering to the αβ interface between the PEG-rich α phase and the dextran-rich β phase as observed by STED microscopy.[11] The image displays a top view from the α phase onto the αβ interface. The number of nanotubes is controlled by the membrane excess area released by osmotic deflation of the vesicle and stored in the tubes. The bright spots represent crossing points of the adhering nanotubes. Scale bar: 2 μm.

their mean curvature to the spontaneous curvature and then do not contribute to the bending energy of the membrane. As a consequence, the overall tube length increases for a larger reduction of vesicle volume or for a larger increase in membrane area. All nanotubes will eventually adhere to the αβ interface. A particularly dense layer of nanotubes as observed by STED microscopy is displayed in Fig. 31. The bright spots correspond to crossing points, at which several nanotubes cross each other during the adhesion process.

14 Summary and outlook

In this paper, we addressed the complex remodeling of biomembranes and vesicles arising from their interactions with condensate droplets. The droplets are formed by aqueous phase separation within the exterior or interior solution. In both cases, the droplets may wet the membrane partially or completely as shown in Fig. 3 and 4 for exterior and interior phase separation, respectively. The reduction of vesicle volume by osmotic deflation and the increase of membrane area by illumination can lead to complete engulfment of the droplets as in Fig. 5, 6, and 24 or, alternatively, to the formation of nanotubes as in Fig. 7–10.

As explained in Section 8, the vesicle–droplet system follows the pathway of complete engulfment when the interfacial tension $\Sigma_{\alpha\beta}$ of the condensate droplets is large compared to the curvature-elastic tensions $\sigma_{\alpha\gamma}$ and $\sigma_{\beta\gamma}$ of the two membrane segments whereas nanotubes are formed if one of the curvature-elastic tensions is large compared to the interfacial tension. Close to a critical demixing point, the interfacial tension $\Sigma_{\alpha\beta}$ vanishes which implies that one of the membrane segments prefers to form nanotubes according to eqn (10).

For both complete engulfment and nanotubulation, the droplet volumes and the membrane area also have to fulfill certain geometric constraints.

The complete engulfment of condensate droplets by a vesicle membrane as in Fig. 5, 6, and 24 leads to the formation of closed membrane necks, which represents the first step for the endocytic uptake of the droplet by the vesicle. The second step of endocytosis is provided by the fission of the closed membrane neck. This two-step process of endocytosis has been observed in molecular dynamics simulations of nanovesicles interacting with nanodroplets as displayed in Fig. 12 and described in Section 9. The simulations also revealed that the engulfment of the condensate droplet can lead to a closed membrane neck with an unusual tight-lipped shape as in Fig. 13, thereby preventing neck fission and vesicle division.

The closure of membrane necks is further elucidated in Section 10 by identifying several distinct pathways for the axisymmetric closure of contact line necks. These pathways include the displacement of the contact line neck from the waistline of the closing neck as in Fig. 14 and the elongation of the neck into an extended nanotube as in Fig. 15.

On the micrometer scale, the partially wetted vesicle membranes exhibit an apparent kink along the contact line as well as three apparent contact angles as in Fig. 16. On the nanometer scale, the vesicle membranes are smoothly curved along the contact line, see Fig. 19, which leads to two intrinsic contact angles as in Fig. 18. The apparent contact angles can be measured by phase-contrast microscopy (Fig. 20), the intrinsic contact angles can be computed from the apparent ones *via* eqn (31) and measured by STED microscopy (Fig. S11a, ESI†).

Along the contact line, the interfacial tension $\Sigma_{\alpha\beta}$ is balanced by the segment tensions $\Sigma^{m}_{\alpha\gamma}$ and $\Sigma^{m}_{\beta\gamma}$ as in Fig. 17 and 18. The force balance between the three surface tensions defines a two-dimensional force balance regime (Fig. 21), which can be used to distinguish and classify the morphological transitions of vesicle–droplet systems (Fig. 23). Examples include complete-to-partial wetting transitions (Fig. 10 and Fig. S5, ESI†), transitions from complete wetting by one aqueous phase to complete wetting by the other aqueous phase (Fig. 22), complete engulfment of condensate droplets (Fig. 5 and 6), light-controlled switching between partial and complete engulfment (Fig. 24) and the formation of tensionless membrane segments (Fig. 25).

For partial wetting, the nanotubes eventually adhere to the αβ interface as displayed in Fig. 9, 10b, 26, and 31. These adhering nanotubes can transform into double-membrane sheets as described in Section 13. One example for such a tube-to-sheet transformation is shown in Fig. 27, one example for the reverse sheet-to-tube transformation in Fig. 28. The presence of tubes and sheets on the same vesicle reveals a bistable free energy landscape with two local free energy minima corresponding to tubes and sheets, respectively. The transformations between tubes and sheets arises from the competition between the negative adhesion free energy, which is proportional to the interfacial tension $\Sigma_{\alpha\beta}$ of the αβ interface, and the curvature-elastic tensions, $\sigma_{\alpha\gamma}$ and $\sigma_{\beta\gamma}$, of the two weakly curved faces of the sheet. If the interfacial tension $\Sigma_{\alpha\beta}$ is large and satisfies eqn (33), the tube is transformed into a sheet as in Fig. 27. On the other hand, if the interfacial tension is small as in eqn (34), the sheet is transformed into a tube as in Fig. 28.

In summary, condensate droplets interacting with biomembranes and vesicles provide fascinating soft matter systems which exhibit unusual elastic properties and remodeling processes. During the last couple of years, many aspects of these processes have been elucidated but much remains to be done.

So far, the distinction between segregative and associative phase separation of aqueous solutions in terms of the number of critical demixing points at constant temperature (Section 2) has been confirmed for a few aqueous two-phase systems, see Fig. 1 and 2 as well as Fig. S1–S3 (ESI†), but should be valid in general.

Likewise, the examples for the remodeling behavior of vesicle–droplet systems, such as complete engulfment, nanotubulation, and endocytosis in Sections 5, 6, and 9 were all obtained for lipid vesicles. However, all remodeling phenomena described here should also be accessible to other vesicles such as polymersomes assembled from amphiphilic block-copolymers,[62,63] dendrimersomes assembled from amphiphilic dendrimers,[64,65] and giant plasma membrane vesicles as produced by chemical blebbing of eukaryotic cells.[66–69]

As described in Section 11.5, membranes and vesicles should be completely wetted by condensate droplets in the vicinity of a critical demixing point and then undergo a complete-to-partial wetting transition at a certain tie line further away from this critical point. This wetting behavior should apply to all aqueous two-phase systems even though it has only been observed, so far, for PEG–dextran (Fig. 10) and glycinin–NaCl solutions (Fig. 22). It then follows that associative phase diagrams, which exhibit two critical points, also exhibit two distinct transitions from complete to partial wetting at constant temperature. Wetting transitions of two coexisting liquid phases in contact with a rigid substrate or a macroscopic liquid–liquid interface have been studied for a long time[60,70–72] but it seems that no such system has been observed to undergo two distinct wetting transitions at constant temperature.

In Sections 9 and 10, molecular dynamics simulations and the theory of curvature elasticity have been used to identify distinct morphological pathways for the closure of membrane necks during endocytic and exocytic engulfment. So far, only the elongation of membrane necks into nanotubes has been observed in experiment (Fig. 15) but neither the axisymmetric pathway, in which the contact line moves away from the closing neck (Fig. 14) nor the strongly non-axisymmetric pathway, in which the neck attains a tight-lipped shape (Fig. 13) have been examined experimentally. For the relative displacement of contact line and membrane neck, one possible approach is to distinguish the two membrane segments by different fluorescent labels and then follow the closure of open necks by confocal microscopy. To identify tight-lipped necks, super-resolution microscopy such as STED should be rather useful.

The shapes of membrane nanotubes, which adhere to the αβ interface as in Fig. 26, remain to be studied in a systematic manner. One aspect that has been ignored in Fig. 26 is that the membrane's mean curvature is discontinuous across the contact line as in eqn (11) and (15). These discontinuities will deform the cross-sections of the membrane nanotubes. Both STED microscopy and molecular dynamics simulations could be applied to determine these tubular shapes.

Another interesting process which has hardly been studied is the nucleation of condensate droplets at vesicle membranes. From the theoretical point of view, this nucleation process should strongly depend on the droplet-induced spontaneous curvature, which can be positive or negative. So far, systematic studies of this process by experiments or simulations are still missing but would be highly desirable.

Finally, the remodeling processes described here for biomimetic soft matter systems consisting of fluid membranes and condensate droplets should also apply, at least in principle, to the behavior of cellular membranes and biomolecular condensates *in vivo*. In practice, the *in vivo* behavior is, however, more difficult to understand in a systematic and quantitative manner because both the membranes and droplets can interact with cytoskeletal filaments and motors, which couple the vesicle–droplet systems to exergonic chemical reactions such as nucleotide hydrolysis.

Conflicts of interest

There are no conflicts to declare.

Note added in proof

The lab of Petra Schwille has recently introduced tunable DNA condensates with photosensitve DNA-lipid linkers, by which one can control contact angles and budding transformations, see N. Kaletta, *et al*.[73]

Data availability

This perspective extends the theory of fluid elasticity to analyze and elucidate the results of recent experimental studies and computer simulations about the interactions of biomembranes and vesicles with condensate droplets. All experimental and simulation data are published and available in the combined list of references for the main text and the ESI.†

Acknowledgements

I thank all my collaborators for enjoyable interactions, Rumiana Dimova and Petra Schwille for stimulating discussions as well as Ziliang Zhao for STED microscopy images and Juan Iglesias-Artola for ref. 29. This research was conducted within the Max Planck School Matter to Life supported by the German Federal Ministry of Education and Research (BMBF) in collaboration with the Max Planck Society and the Max Planck Institute of Colloids and Interfaces. Open Access funding provided by the Max Planck Society.

References

1 P. A. Albertsson, *Partition of Cell Particles and Macromolecules: Separation and Purification of Biomolecules, Cell Organelles Membranes, and Cells in Aqueous Polymer Two-Phase Systems and Their Use in Biochemical Analysis and Biotechnology*, Wiley, 3rd edn, 1986.
2 L. Piculell and B. Lindman, *Adv. Colloid Interface Sci.*, 1992, **41**, 149–178.
3 J. Esquena, *Curr. Opin. Colloid Interface Sci.*, 2016, **25**, 109–119.
4 R. Lipowsky, *Faraday Discuss.*, 2013, **161**, 305–331.
5 R. Lipowsky, *J. Phys. Chem. B*, 2018, **122**, 3572–3586.
6 R. Lipowsky, *Membranes*, 2023, **13**, 223.
7 M. Helfrich, L. Mangeney-Slavin, M. Long, K. Djoko and C. Keating, *J. Am. Chem. Soc.*, 2002, **124**, 13374–13375.
8 Y. Li, R. Lipowsky and R. Dimova, *J. Am. Chem. Soc.*, 2008, **130**, 12252–12253.
9 Y. Li, R. Lipowsky and R. Dimova, *Proc. Natl. Acad. Sci. U. S. A.*, 2011, **108**, 4731–4736.
10 Y. Liu, J. Agudo-Canalejo, A. Grafmüller, R. Dimova and R. Lipowsky, *ACS Nano*, 2016, **10**, 463–474.
11 Z. Zhao, D. Roy, J. Steinkühler, T. Robinson, R. Lipowsky and R. Dimova, *Adv. Mater.*, 2022, **34**, 2106633.
12 A. Mangiarotti, N. Chen, Z. Zhao, R. Lipowsky and R. Dimova, *Nat. Commun.*, 2023, **14**, 2809.
13 A. Mangiarotti, M. Aleksanyan, M. Siri, T.-W. Sun, R. Lipowsky and R. Dimova, *Adv. Sci.*, 2024, **11**, 2309864.
14 A. Mangiarotti and R. Dimova, *Annu. Rev. Biophys.*, 2024, **53**, 319–341.
15 Z. Zhao, V. Satarifard, R. Lipowsky and R. Dimova, *Proc. Natl. Acad. Sci. U. S. A.*, 2024, **121**, e2321579121.
16 V. Satarifard, A. Grafmüller and R. Lipowsky, *ACS Nano*, 2018, **12**, 12424–12435.
17 R. Ghosh, V. Satarifard and R. Lipowsky, *Nat. Commun.*, 2023, **14**, 615.
18 R. Lipowsky, R. Ghosh, V. Satarifard, A. Sreekumari, M. Zamaletdinov, B. Różycki, M. Miettinen and A. Grafmüller, *Biomolecules*, 2023, **13**, 926.
19 R. Lipowsky, *Faraday Discuss.*, 2025, DOI: 10.1039/D4FD00184B.
20 C. Love, J. Steinkühler, D. T. Gonzales, N. Yandrapalli, T. Robinson, R. Dimova and T.-Y. D. Tang, *Angew. Chem.*, 2020, **132**, 6006–6013.
21 M. G. F. Last, S. Deshpande and C. Dekker, *ACS Nano*, 2020, **14**, 4487–4498.
22 Y. Zhang, Y. Chen, X. Yang, X. He, M. Li, S. Liu, K. Wang, J. Liu and S. Mann, *J. Am. Chem. Soc.*, 2021, **143**, 2866–2874.
23 F. P. Cakmak, A. M. Marianelli and C. D. Keating, *Langmuir*, 2021, **37**, 10366–10375.
24 T. Lu, S. Liese, L. Schoenmakers, C. A. Weber, H. Suzuki, W. T. S. Huck and E. Spruijt, *J. Am. Chem. Soc.*, 2022, **144**, 13451–13455.

25 C. P. Brangwynne, C. R. Eckmann, D. S. Courson, A. Rybarska, C. Hoege, J. Gharakhani, F. Jülicher and A. A. Hyman, *Science*, 2009, **324**, 1729–1732.
26 S. F. Banani, H. O. Lee, A. A. Hyman and M. K. Rosen, *Nat. Rev. Mol. Cell Biol.*, 2017, **18**, 285–295.
27 N. Chen, Z. Zhao, Y. Wang and R. Dimova, *ACS Macro Lett.*, 2020, **9**, 1844–1852.
28 A. W. Fritsch, A. F. Diaz-Delgadillob, O. Adame-Arana, C. Hoege, M. Mittasch, M. Kreysing, M. Leaver, A. A. Hyman, F. Jülicher and C. A. Weber, *Proc. Natl. Acad. Sci. U. S. A.*, 2021, **118**, e2102772118.
29 A. W. Fritsch, J. M. Iglesias-Artola and A. A. Hyman, *bioRxiv*, 2024, preprint, DOI: 10.1101/2024.10.02.616352.
30 L.-P. Bergeron-Sandoval, S. Kumar, H. K. Heris, C. Chang, C. E. Cornell, S. L. Keller, P. François, A. Hendricks, A. J. Ehrlicher, R. V. Pappu and S. W. Michnick, *Proc. Natl. Acad. Sci. U. S. A.*, 2021, **118**, e2113789118.
31 W. T. Snead, A. P. Jalihal, T. M. Gerbich, I. Seim, Z. Hu and A. S. Gladfelter, *Nat. Cell Biol.*, 2022, **24**, 461–470.
32 B. Gouveia, Y. Kim, J. W. Shaevitz, S. Petry, H. A. Stone and C. P. Brangwynne, *Nature*, 2022, **609**, 255–264.
33 F. Yuan, C. T. Lee, A. Sangani, J. R. Houser, L. Wang, E. M. Lafer, P. Rangamani and J. C. Stachowiak, *Sci. Adv.*, 2023, **9**, eadg3485.
34 K. Pombo-García, O. Adame-Arana, C. Martin-Lemaitre, F. Jülicher and A. Honigmann, *Nature*, 2024, **632**, 647–655.
35 C. D. Crowe and C. D. Keating, *Interface Focus*, 2018, **8**, 20180032.
36 Y. Liu, R. Lipowsky and R. Dimova, *Langmuir*, 2012, **28**, 3831–3839.
37 R. Ghosh, V. Satarifard, A. Grafmüller and R. Lipowsky, *ACS Nano*, 2021, **15**, 7237–7248.
38 S. Bonnassieux, R. Pandya, D. A. Skiba, D. Degoulange, D. Petit, P. Seem, R. P. Cowburn, B. M. Gallant and A. Grimaud, *Faraday Discuss.*, 2024, **253**, 181–192.
39 C. Pernpeintner, J. A. Frank, P. Urban, C. R. Roeske, S. D. Pritzl, D. Trauner and T. Lohmüller, *Langmuir*, 2017, **33**, 4083–4089.
40 V. N. Georgiev, A. Grafmüller, D. Bléger, S. Hecht, S. Kunstmann, S. Barbirz, R. Lipowsky and R. Dimova, *Adv. Sci.*, 2018, **5**, 1800432.
41 R. Osserman, *Bull. Am. Math. Soc.*, 1978, **84**, 1182–1238.
42 S. Hildebrandt and A. Tromba, *Mathematics and Optimal Form*, American Scientific Library, New York, NY, USA, 1985.
43 Y. Li, H. Kusumaatmaja, R. Lipowsky and R. Dimova, *J. Phys. Chem. B*, 2012, **116**, 1819–1823.
44 R. Dimova and R. Lipowsky, *Adv. Mater. Interfaces*, 2017, **4**, 1600451.
45 R. Lipowsky, *Physics of Biological Membranes*, Springer, 2018, pp. 1–44.
46 R. Lipowsky, *The Giant Vesicle Book*, Taylor & Francis, 2019, ch. 5, pp. 73–168.
47 T. Bhatia, J. Agudo-Canalejo, R. Dimova and R. Lipowsky, *ACS Nano*, 2018, **12**, 4478–4485.
48 J. Steinkühler, R. L. Knorr, Z. Zhao, T. Bhatia, S. Bartelt, S. Wegner, R. Dimova and R. Lipowsky, *Nat. Commun.*, 2020, **11**, 905.
49 D. Roy, J. Steinkühler, Z. Zhao, R. Lipowsky and R. Dimova, *Nano Lett.*, 2020, **20**, 3185–3191.
50 J. W. Cahn and J. E. Hilliard, *J. Chem. Phys.*, 1958, **28**, 258–267.
51 A. Derzhanski, A. G. Petrov and M. D. Mitov, *Ann. Phys.*, 1978, **3**, 297.
52 S. Lorenzen, R.-M. Servuss and W. Helfrich, *Biophys. J.*, 1986, **50**, 565–572.
53 M. Hu, J. J. Briguglio and M. Deserno, *Biophys. J.*, 2012, **102**, 1403–1410.
54 M. Andes-Koback and C. D. Keating, *J. Am. Chem. Soc.*, 2011, **133**, 9545–9555.
55 H. Kusumaatmaja, Y. Li, R. Dimova and R. Lipowsky, *Phys. Rev. Lett.*, 2009, **103**, 238103.
56 F. Jülicher and R. Lipowsky, *Phys. Rev. E: Stat. Phys., Plasmas, Fluids, Relat. Interdiscip. Top.*, 1996, **53**, 2670–2683.
57 R. Lipowsky, *Eur. Phys. J. E: Soft Matter Biol. Phys.*, 2024, **47**, 4.
58 R. Lipowsky, *Adv. Biol.*, 2022, **6**, 2101020.
59 J. Rowlinson and B. Widom, *Molecular Theory of Capillarity*, Oxford University Press, Oxford, 1989.
60 J. W. Cahn, *J. Chem. Phys.*, 1977, **66**, 3667–3672.
61 M. Moldover and J. Cahn, *Science*, 1980, **207**, 1073–1075.
62 B. M. Discher, Y.-Y. Won, D. S. Ege, J. C.-M. Lee, F. S. Bates, D. E. Discher and D. A. Hammer, *Science*, 1999, **284**, 1143–1146.
63 E. Rideau, R. Dimova, P. Schwille, F. R. Wurm and K. Landfester, *Chem. Soc. Rev.*, 2018, **47**, 8572–8610.
64 V. Percec, D. A. Wilson, P. Leowanawat, C. J. Wilson, A. D. Hughes, M. S. Kaucher, D. A. Hammer, D. H. Levine, A. J. Kim, F. S. Bates, K. P. Davis, T. P. Lodge, M. L. Klein, R. H. DeVane, E. Aqad, B. M. Rosen, A. O. Argintaru, M. J. Sienkowska, K. Rissanen, S. Nummelin and J. Ropponen, *Science*, 2010, **328**, 1009–1014.
65 N. Y. Kostina, K. Rahimi, Q. Xiao, T. Haraszti, S. Dedisch, J. P. Spatz, U. Schwaneberg, M. L. Klein, V. Percec, M. Möller and C. Rodriguez-Emmenegger, *Nano Lett.*, 2019, **19**, 5732–5738.
66 R. E. Scott, *Science*, 1976, **194**, 743–745.
67 T. Baumgart, A. T. Hammond, P. Sengupta, S. T. Hess, D. A. Holowka, B. A. Baird and W. W. Webb, *Proc. Natl. Acad. Sci. U. S. A.*, 2007, **104**, 3165–3170.
68 H. Keller, M. Lorizate and P. Schwille, *ChemPhysChem*, 2009, **10**, 2805–2812.
69 J. Steinkühler, P. Fonda, T. Bhatia, Z. Zhao, F. S. C. Leomil, R. Lipowsky and R. Dimova, *Adv. Sci.*, 2021, **8**, 2102109.
70 R. Lipowsky, *Phys. Rev. Lett.*, 1984, **52**, 1429–1432.
71 H. Gau, S. Herminghaus, P. Lenz and R. Lipowsky, *Science*, 1999, **283**, 46–49.
72 D. Bonn, J. Eggers, J. Indekeu, J. Meunier and E. Rolley, *Rev. Mod. Phys.*, 2009, **81**, 739–805.
73 N. Kaletta, S. Burick, Y. Qudbuddin and P. Schwille, *Adv. Sci.*, 2025, e15510.

